To the Graduate Council:

I am submitting herewith a thesis written by Thomas H. Walloschek entitled "Coaxial Thermal Pulsed Plasma Thrusters." I have examined the final copy of this thesis for form and content and recommend that it be accepted in partial fulfillment of the requirements for the degree of Master of Science, with major in Aerospace Engineering.

Dr. Dennis Keefer, Major Professor

We have read this thesis
and recommend its acceptance:

Accepted for the Council:

Associate Vice Chancellor and
Dean of the Graduate School

COAXIAL THERMAL PULSED PLASMA THRUSTERS

A Thesis

Presented for the

Master of Science

Degree

The University of Tennessee, Knoxville

Thomas H. Walloschek

May 1998

DEDICATION

Ich widme diese thesis meiner Familie,

besonders meinen Eltern

Heinrich Walloschek

und

Renate Walloschek

die mir mit Ihrer Liebe und

Unterstuetzung bei all meinen Vorhaben

alles ermoeglicht haben.

ACKNOWLEDGEMENTS

I would like to thank my advisor Dr. Dennis Keefer for his guidance, advice and many discussions during my education here at the University of Tennessee Space Institute. I also appreciate the assistance and support of the other professors on my committee, Dr. Montgomery Smith and Dr. Gary Flandro. I thank Mr. Newton Wright for his help in setting up and running the experiment; he always had a solution if something did not work.

This work was funded by the AFOSR under contract numbers F49620-97-1-0223 and F49620-94-1-0331.

I also want to thank Prof. Messerschmid, the director of the Institute for Space Systems at the University of Stuttgart, who allowed me to attend UTSI for my first thesis. I thank Prof. Auweter-Kurtz, head of the Elecrtic Propulsion Systems and Plasma Techniques at the University of Stuttgart who was my advisor in Germany, for her advice and support.

Thanks also to all my new friends especially my roommates, who made the time here at UTSI enjoyable.

ABSTRACT

This thesis investigates the operation and performance of a thruster design that utilizes the discharge within a conical cavity existing of a copper cathode, a plastic propellant and a tungsten anode to produce a pulse of plasma. Analysis suggests that thermal processes are more important than electromagnetic forces in the acceleration of the plasma propellant. A pulsed plasma thruster experiment was designed, fabricated and operated to test the hypothesis and to investigate the effects of discharge energy, nozzle design and propellant material. A capacitive discharge circuit was designed and fabricated. This circuit was used to power a thruster design which utilized different solid plastic propellants. Two different propellants were used for the experiments to test this hypothesis, Teflon $(CF_2)_n$ and polyethylene $(CH_2)_n$. The polyethylene was expected to give a higher specific impulse because of its lower average molecular weight.

The exhaust velocity was measured using a two beam laser interferometer. In order to verify the correctness of the results with the interferometer also a high speed camera was used to take pictures of the exhaust plume from which the velocity could also be measured. The mass ablation was also measured to give an insight in the ablation behavior of the thruster of a broader initial stored energy range. Besides the values mentioned above we also measured the voltage and current input into the thruster. Spectrometer data of the exhaust plume were also recorded.

The results of the experiments supported the hypothesis. The specific impulse and the velocities of the polyethylene propellant with up to 3000 s were approximately twice as high as the values for the Teflon propellant with up to 1450s. We also found that the larger nozzle worked much better than the small nozzle, which supported the hypothesis that mainly electrothermal processes accelerated the propellants as the plasma was better expanded. Thrust efficiencies up to 10 % for polyethylene and 5 % for Teflon were measured using the large nozzle.

TABLE OF CONTENTS

CHAPTER PAGE

1. INTRODUCTION 1
   - 1.1 Historical Background 1
   - 1.2. Overview 4
   - 1.3 Electric Thrusters 5
     - 1.3.1 Magneto Plasma Dynamic Thrusters (MPD) 6
       - 1.3.1.1 Pulsed Thrusters 6
       - 1.3.1.2 Quasistationary Thrusters 7
       - 1.3.1.3 Continuously Operated Thrusters 8
     - 1.3.2 Electrostatic Thrusters 8
       - 1.3.2.1 Kaufman-Thrusters 9
       - 1.3.2.2 Radiofrequency-Ion-Thrusters (RIT) 9
       - 1.3.2.3 Contact Ionization Thrusters 10
       - 1.3.2.4 Field-Emission Thrusters 10
     - 1.3.3 Electrothermal Thursters 10
       - 1.3.3.1 Resistojets 10
       - 1.3.3.2 Arcjets 11
       - 1.3.3.3 Coaxial Thermal Pulsed Plasma Thrusters 12

2. THEORY 14
   - 2.1 Electric Circuit 14
   - 2.2 Electromagnetic/ Electrothermal Acceleration 18
   - 2.3 Electron Number Density 25

CHAPTER PAGE

3. EXPERIMENTS 30

3.1 Experimental Setup 30

3.2 Thruster 33

3.3 Power Supply 37

3.4 Data Acquisition Equipment 40

4. ANALYSIS AND RESULTS 46

4.1 Mass Ablation 48

4.2 Velocity Measurements 54

4.3 Impulse Bit and Specific Impulse 60

4.4 Thrust Power and Efficiency 64

4.5 Interferometer Analysis 66

4.6 Power and Dissipated Energy 76

4.7 Electron Number Density 80

4.8 Spectrometer Data 83

5. SUMMARY/ CONCLUSIONS 84

LIST OF REFERENCES 89

BIBLIOGRAPHY 93

APPENDIX: PICTURES OF THE EXPERIMENT 96

VITA 101

LIST OF TABLES

TABLE		PAGE
Table 4.1:	Listing of experimental configurations with measured Parameters	47
Table 4.1.1:	Listing of resulting mass ablation data	51
Table 4.2.1:	Summary of the average exhaust velocities for a the ½ inch (small) nozzle and the ¾ inch (large) nozzle	57
Table 4.2.2:	Exhaust velocity ratios for polyethylene compared to Teflon	59

LIST OF FIGURES

FIGURE		PAGE
Figure 1.3.1:	Schematic of a coaxial thermal pulsed plasma thruster	12
Figure 2.1.1:	Schematic of the main energy storage unit	15
Figure 2.3.1:	Schematic of the paths of the reference and measurement beams with d as the effective path length	26
Figure 3.1.1:	Schematic of the experimental setup	31
Figure 3.2.1:	Drawing set for the ¾ inch (large) nozzle	34
Figure 3.2.2:	Drawing set for the ½ inch (small) nozzle	35
Figure 3.2.3:	Breakdown path of the arc from the cathode to the anode	36
Figure 3.3.1:	Diagram of the ignition circuit	39
Figure 3.3.2:	Schematic of the main ignition unit	39
Figure 3.4.1:	Schematic of the interferometer setup	42
Figure 4.1.1:	Measured mass ablation per shot as a function of initial stored energy	48
Figure 4.1.2:	Energy flux as a function of initial stored energy	53
Figure 4.2.1:	Average exhaust velocity as a function of initial stored energy a) small nozzle, b) large nozzle	56
Figure 4.2.2:	Ratios of the exhaust velocities of polyethylene compared to Teflon as a function of initial stored energy	59

Figure 4.3.1: Impulse bit as a function of initial stored energy: a) small nozzle, b) large nozzle 61

Figure 4.3.2: Specific impulse as a function of initial stored energy: a) small nozzle, b) large nozzle 63

Figure 4.4.1: Thrust kinetic energy for a single pulse as a function of initial stored energy: a) small nozzle, b) large nozzle 65

Figure 4.4.2: Thrust efficiency as a function of initial stored energy: a) small nozzle, b) large nozzle 67

Figure 4.5.1: Oscilloscope data with significant truncation points 69

Figure 4.5.2: Current, voltage and demodulated phase shift data of a Teflon shot with an initial stored energy of 198J for the large nozzle . 72

Figure 4.5.3: Correlation curve of the phase shift data of the Teflon shot in Figure 4.5.2 72

Figure 4.5.4: Current, voltage and demodulated phase shift data of a polyethylene shot with an initial stored energy of 198J for the large nozzle 73

Figure 4.5.5: Correlation curve of the phase shift data of the polyethylene shot in Figure 4.5.4 73

Figure 4.6.1: Power and energy thruster input as a function of time for a Teflon shot with an initial stored energy of 198J for the large nozzle 77

Figure 4.6.2: Power and energy thruster input as a function of time for a polyethylene shot with an initial stored energy of 198J for the large nozzle 77

Figure 4.7.1: Electron number density as a function of time for each first beam of a Teflon and a polyethylene shot with an initial stored energy of 198 J for the large nozzle 82

Figure 4.8.1: Spectroscopic data for a Teflon and a polyethylene shot with an initial stored energy of 132.8 J for the large nozzle 83

LIST OF PLATES

PLATE		PAGE
Plate 4.5.1:	Picture of the exhaust plume of a Teflon shot at an initial stored energy level of 198 J for the large nozzle with an interframe time of 1 μs	70
Plate 4.5.2:	Picture of the exhaust plume of a polyethylene shot at an initial stored energy level of 198 J for the large nozzle with an interframe time of 1 μs	70
Plate A1:	Experimental Setup	97
Plate A2:	Picture of the thruster designed for the experiment	98
Plate A3:	Large nozzle (left) compared to small nozzle (right)	98
Plate A4:	Picture of the small nozzle with the soot layer at the inner nozzle walls	99
Plate A5:	Picture of the ablation area of the propellant for the small nozzle	99
Plate A6:	Picture of the ablation area of the propellant for the large nozzle	99
Plate A7:	Picture of a shot as seen by an observer	100

CHAPTER 1

INTRODUCTION

1.1 HISTORICAL BACKGROUND

The primary source of energy used to leave the earth's surface and get into space these days is provided by chemical propulsion devices. Chemical propulsion represents high impulse missions and allows us to transport payloads into low earth orbits or to leave earth's gravity. At this point in time a huge amount of fuel is consumed compared to a relatively small payload. The reason for this is the nature of chemical fuels with their small energy content that restricts exhaust velocities to approximately 4 to 5 km/s and the specific impulse I_{sp} to approximately 450 s for liquid rocket motors and 250 s for solid rocket motors.

This problem was recognized several decades ago. Robert H. Goddard [1], in 1906, or Professor Herman Oberth , in 1929, in his book "Man into Space" [2] thought about possible ways to overcome these restrictions and expressed several ideas for electric propulsion as an additional propulsion device to improve the overall efficiency of a spacecraft. At that time, no real space program existed. The first serious research projects were started in the late fifties and early sixties, sparked by the development of rockets in the second world war that demonstrated that space travel was possible. Ernst Stuhlinger [3-5], with his research studies, showed the advantages of electrical

propulsion using upcoming future space power sources like solar arrays and nuclear fission. Worldwide research in the field of electric propulsion began in the 1960's. Since then, several types of electric thrusters were developed, investigated and flown on spacecraft.

Today we distinguish between three main groups of electrical propulsion that mainly differ in the manner of acceleration: electromagnetic propulsion, electrothermal propulsion and electrostatic propulsion. A good definition for these three concepts is given in Robert G. Jahn's book "Physics of Electric Propulsion" [6]:

1. "*Electrothermal propulsion,* wherein the propellant gas is heated electrically, then expanded in a suitable nozzle" [6].
2. "*Electrostatic propulsion,* wherein the propellant is accelerated by direct application of electric body forces to ionized particles" [6].
3. "*Electromagnetic propulsion,* wherein an ionized propellant stream is accelerated by interactions of external and internal magnetic fields with electric current driven through the stream" [6].

These devices can again be separated into different classes defined by their mode of operation. Thruster operation can be continuous or stationary, quasistationary or pulsed.

As mentioned above, the exhaust velocity of chemical propulsion is restricted to approximately 4 to 5 km/s, which is low compared to electrical propulsion. With today's electric propulsion devices and propellants, we can achieve exhaust velocities

up to 8 km/s with resistojets, 15 km/s with thermal plasma thrusters, 30 km/s with magneto plasma dynamic thrusters, and the highest exhaust velocity that can be achieved is with electrostatic thrusters with up to 60 km/s [7]. The specific impulse range of electric thrusters varies from 500 s up to 10000s. The different kinds of thrusters are explained later in section 1.3.

Several kinds of thrusters have been flown on satellites. One of the first successful experiments was a ballistic flight of an American test capsule that took place in 1964 with an electrostatic ion engine [8]. Since approximately 1980, the work in the USA has concentrated mainly on continuously driven electrothermal and electromagnetic devices and so called pulsed plasma thrusters (PPT's). The electrothermal and electromagnetic thrusters are operated at power levels up to 30 kW [7]. An example for the use of PPT's was the LES 6 (Lincoln Laboratory Satellite), on which the PPT successfully provided east-west station keeping [9].

Since the 1970's, several kinds of thrusters were also developed and tested in the USSR. Japan has also done work on thermal and magnetoplasmadynamic (MPD) thrusters for several years. A PPT was tested since 1980 on the satellite MS-T4 [7].

In Europe, electric propulsion research has been mainly performed in Germany at the University of Stuttgart (Institute for Space Systems) since 1980. Now work is also done in Italy at BPD Difasio e Spazio. At Stuttgart, continuously operated MPD thrusters in the power range of 100 kW up to 1 MW and thermal plasma thrusters in the power range of 1 kW up to 100 kW were tested and developed [7]. Italy focused

on quasistationary pulsed MPD thrusters with Teflon as the propellant, smaller thermal thrusters and large quasistationary thrusters [7].

1.2 OVERVIEW

With the improvement of spacecraft power supplies and the increasing need for satellite technology, interest in electric propulsion has grown again in the last two decades. Better solar arrays with a higher efficiency now exist and also available are fission reactors that are small enough to be integrated into a spacecraft, but only very rarely used mainly for deep space missions. Today, especially with the upcoming Mars missions, an increasing amount of research in higher thrust electric propulsion is being done, and work on nuclear thermal reactors has intensified. But as electric power is still restricted in most missions, only thrusters in the lower power range are presently used in space applications. The main advantage of electric propulsion is the simplicity and much lower fuel consumption of the thrusters compared to chemical propulsion devices, which enables the spacecraft to carry a larger payload and to operate over a much longer range of time.

Another important advantage over chemical devices is the ability of several thrusters to work with different propellants and different power levels. Due to this fact, one can precisely choose the thruster with the desired thrust, specific impulse, propellant, and power level for the needs of the mission and spacecraft. Also with the

small thrust levels and burn duration available to electric rockets, very high precision maneuvers are possible, e.g. minute fraction of a degree attitude changes can be made.

The areas in which electric propulsion is used on big satellites are mainly trajectory control (e.g. east-west station keeping and north-south station keeping) on geostationary and high earth orbit satellites, which lengthens their lifetime up to 10 years and longer. Electric thrusters are also ideal for use in smaller satellites, as orbit changes are also possible. For spacecraft in low earth orbits, like space stations, big satellites, or experimental platforms, electric thrusters can be used to counteract the resistance due to the residual atmosphere and to change their flight trajectory.

With growing interest in the development of new reusable transportation systems for manned space flight, a new area arose in which electric propulsion is mainly used as a plasma source in plasma wind tunnels. In these wind tunnels, the conditions at reentry into a planet's atmosphere is simulated to test and verify new materials for the heat protection of spacecraft [7].

1.3 ELECTRIC THRUSTERS [7,10]

Electric propulsion can be separated into three areas as mentioned above, electrothermal thrusters, electromagnetic thrusters and electrostatic thrusters. Electro-thermal thrusters can again be distinguished into several types depending on their power source and heating mechanism for the propellant gas. Up to this point, work

has been done on nuclear-thermal, solar-thermal, electrothermal and laser thrusters. Electrothermal thrusters can have different energy sources like solar electric or nuclear power [10]. The propellant gas of a thermal thruster can be heated over resistors or over an arc. Most of the existing thermal thrusters are operated continuously. This thesis concentrates on a new kind of thermal thruster, a pulsed plasma thruster (PPT) with solid propellants designed like a coaxial cable, with a center conductor, a plastic insulator as propellant and an outer conductor.

Electromagnetic thrusters use magnetic fields for the main acceleration of ionized plasma, and the thermal aspect is only an additional factor. Electromagnetic thrusters can use self-induced magnetic fields for the acceleration of the propellant gas or the additional use of an external magnetic field. Electromagnetic thrusters can be operated, quasistationary, pulsed or continuously.

Electrostatic thrusters (also called ion thrusters) use ions as a working fluid, which are accelerated by electric fields. Several devices differ in the matter of the creation of the ions, and so, one talks about Kaufman-thrusters, contact ionization thrusters, radio frequency ion thrusters, and field emission thrusters.

1.3.1 MAGNETO PLASMA DYNAMIC THRUSTERS (MPD)

1.3.1.1 Pulsed Thrusters

In pulsed thrusters the plasma is accelerated by time-varying magnetic fields. An example is the parallel rail accelerator, with two electrodes mounted parallel to

each other. The propellant is solid and the discharge between the two rails occurs initially over the surface of the propellant and ablates some of it, creating ionized plasma, which is then accelerated by the electromagnetic forces towards the exit. A common propellant used in rail accelerators is Teflon [7]. A thruster of this kind has been flown, the LES-6 pulsed plasma thruster had a thrust efficiency of only 3 % with an I_{sp} of 312 s and an average exhaust velocity of 3180 m/s with the ions accelerated up to 35 km/s [9]. Other research showed that effective exit velocities of approximately 18 km/sec with an overall efficiency of approximately 31% could be achieved [7].

1.3.1.2 Quasistationary Thrusters

In a quasistationary thruster, a several millisecond pulse is created that is longer than the relaxation time or the current rise time of the plasma, so that the arc is stationary for this pulse time. The temperature conditions at the electrode are lower than for stationary operation. Since the burn times of the thruster are very small, the material never gets as hot as in the continuously operated device. Higher currents can be applied, producing larger induced magnetic fields, which raises the thrust quadratically with current. This is important, as the mean power normally available is relatively low on spacecraft. In a pulsed mode, several megawatts can be achieved over the pulse time. Gaseous and solid propellants can be used, where the mean molecular weight of the propellant should be small. Exit velocities up to 30 km/sec

and thrust efficiencies up to 30% can be achieved. Thrusts up to 80 N at approximately 27 kA have been reached [7].

1.3.1.3 Continuously Operated Thrusters

In a continuously operated thruster a stable arc is created from the cathode to the anode, and stationary conditions are reached at the electrodes. The cathode gets sufficiently hot that enough electrons are emitted to enable a continuous arc. These devices normally have a better efficiency than the pulsed devices. Due to the very high permanent power requirements, none of these thrusters have ever been flown on a spacecraft, and more research still has to be done. These devices are at this moment mainly used in plasma wind tunnels.

The most advanced continuously operated MPD's exist, at this point, at the University of Stuttgart. Different kinds of gases and gas mixtures are used as propellants. Effective exhaust velocities up to 14 km/s, thrust efficiencies of 20 % to 30 %, and thrusts of 20 N have been reached. The I_{sp} ranges from 800 s to 4000 s [7, 11].

1.3.2 ELECTROSTATIC THRUSTERS

Heavy ions of mass m_i in the accelerating plasma and a singular stage of ionization of the particles because the thrust is proportional to $(m_i/q_i)^2$ are wanted in electrostatic thrusters [10]. The thrust range reaches from several tenths of a mN up to

several tenths of a N. The specific impulse I_{sp} goes from 3000 s up to 10000 s. Several electrostatic thrusters have reached an overall efficiency of up to 70 % [11].

1.3.2.1 Kaufman-Thruster

The main parts of a Kaufman thruster are again a cathode and an anode. The propellant gas is injected into a chamber, where an arc from the cathode to the anode creates a plasma. The ions of the plasma are then separated from the electrons by an extraction grid and then accelerated by an acceleration grid. A magnetic field keeps the very hot plasma from getting into contact with the chamber walls. The exhaust plume then has to be neutralized by supplying electrons to the particle stream. Thrust levels from about 20 mN up to 0.6 N can be achieved. Several thrusters of this kind have already flown in several countries on several missions [7].

1.3.2.2 Radiofrequency-Ion-Thruster (RIT)

This thruster needs no electrodes for the creation of the plasma but instead uses high frequency radio waves. The ions are separated from the electrons by an extraction grid and then accelerated by an acceleration grid. The particle stream is neutralized by the supply of electrons after the acceleration. RIT thrusters exist with thrust levels of 2 mN up to 200 mN exist [7].

1.3.2.3 Contact Ionization Thrusters

The principle for the ionization of the propellant gas is to bring the propellant in contact with a metal, which works as a catalyst. As the propellant contacts the metal, an electron is given to the metal and the gas becomes ionized. Energy in form of heat has to be supplied to enable the ion to leave the metal surface. No extraction grid is necessary. A problem here is the contamination of the metal. Thrust efficiencies of less than 15 % and thrust levels in the low mN range prevent the use of such thrusters [7].

1.3.2.4 Field-Emission Thrusters

This thruster uses liquid metals as a propellant. From the liquid propellant, ions or colloidal drops are directly created by very high voltages. Exit velocities of over 60 km/s can be reached. The problem of contamination exists in these devices and very little research is done in this field [7].

1.3.3 ELECTROTHERMAL THRUSTERS

1.3.3.1 Resistojets [7,10]

Resistojets are considered thermal propulsion devices, since the propellant gas is heated over resistors. The gas is then accelerated in a so-called Laval nozzle. So far these thrusters are the most similar to chemical thrusters. The electric energy is not directly supplied to the gas, which restricts the exhaust velocities to around 8 km/s.

Another restriction is the temperature limit of the combustion chamber due to the available materials for the heat exchanger. The relationship for the nozzle exit velocity (u_e) as a function of the effective molecular weight (M_{eff}) of the propellant gas and the combustion chamber temperature (T_0) (expansion of the gas into vacuum) is:

$$u_e \propto (T_0/M_{eff})^{1/2} \qquad [7].$$

In order to have good thruster performance, one wants to have a high T_e and a low M_{eff}. Therefore the best propellant is hydrogen as it is the lightest, although several other gases can be used as propellants. Commercial resistojets have used hydrazine as a propellant. The thrust levels of resistojets used so far is in the range of several mN to some N with an I_{sp} of 200 s to 800 s. The thrust efficiency is up to 80%, which is very good compared to many electric propulsion devices [11]. Several thrusters of this kind have already flown on satellites, mainly for attitude control. These devices are desirable due to their relative simplicity and high reliability.

1.3.3.2 Arcjets [7]

This is also a thermal propulsion device, as the propellant gas is heated by an arc. The main parts of an arcjet are the cathode and the anode. The anode forms a pipe with the rear end shaped like a Laval nozzle. The cathode is located at the entrance of the anode through which the propellant gas is fed on its way to the Laval nozzle. An arc between the cathode and the anode is created and the propellant is heated directly though the resistance of the arc. This results in an acceleration of the

gas, which is then expanded through the Laval nozzle. To find the best conditions to operate this thruster, we again can find the very simplified relation for the effective exit velocity u_e is:

$$u_e \propto (T_0/M_{eff})^{1/2} .$$

In order to obtain high exit velocities, again, the temperature of the gas in the combustion chamber should be as high as possible and the mean molecular weight of the working fluid should be small. Exit velocities up to 15 km/s can be achieved with these thrusters. The thrust range of existing thrusters are from 0.05 N up to 5 N, with specific impulses in the range from 400 s to 2000 s and overall efficiencies of 30% to 40 % [11].

1.3.3.3 Coaxial Thermal Pulsed Plasma Thrusters

The coaxial thermal pulsed plasma thruster is manufactured out of a coaxial cable with an outer conductor, a plastic insulator, and a center conductor. A 60 degree inverted cone is machined into this device as shown in Figure 1.3.1.

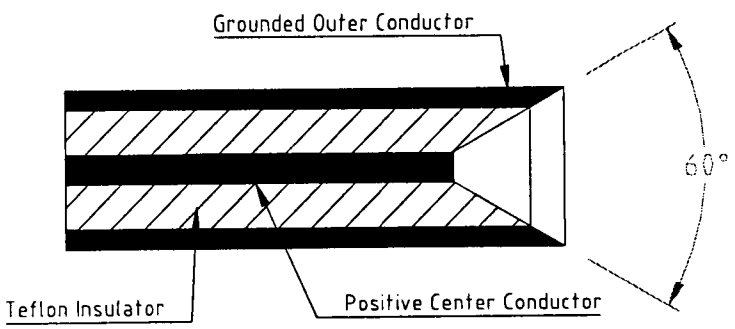

Figure 1.3.1. Schematic of a coaxial thermal pulsed plasma thruster.

The advantage of such thrusters for use in space application is their simplicity. The propellant is a solid propellant, which means that no complicated propellant storage or feeding systems are necessary. As this propulsion device operates in a pulsed mode, the power requirements can be fulfilled with today's space power sources, mainly with solar arrays already used on satellites. The power supply and trigger for such a thruster are also relatively small and with the low propellant consumption and high exhaust velocities the overall weight of the thruster is low, which allows the spacecraft to carry a bigger payload. The pulses are very short, so that a high accuracy for attitude control is guaranteed. Encouraged from earlier theoretical work [12] the model of a coaxial thermal pulsed plasma thruster was created. The discussion of the first experiments and the results are the content of this thesis and are explained in detail in the following chapters.

CHAPTER 2

THEORY

2.1 ELECTRIC CIRCUIT

The power supply we used was a LRC circuit with the configuration shown in Figure 2.1.1. A detailed description and a schematic of the power supply is given in Chapter 3. We used a crowbar shorting switch which in the optimal case would have prevented the capacitor voltage from becoming negative. This meant that after the crowbar switch was closed, only a LR circuit existed and the capacitor was separated from the circuit. To model the behavior of the power supply we assumed an optimal case. For the increasing part of the current and the part before the zero crossing of the voltage we used the equations for an underdamped RLC circuit. After the peak current we used the equations of a LR circuit to match the data recorded from the experiment. With this simulation we were able to predict the approximate values for the inductance and the resistance of the power supply and the thruster.

The decision that we had an underdamped case was based on an estimate of the resistance and inductance of the power circuit. Therefore the approximate inductance of the coaxial low inductance package was calculated with the design measurements, and estimates for the cable inductance were added to get an approximate value. The value for the inductance was compared to the inductance given by the bench mark

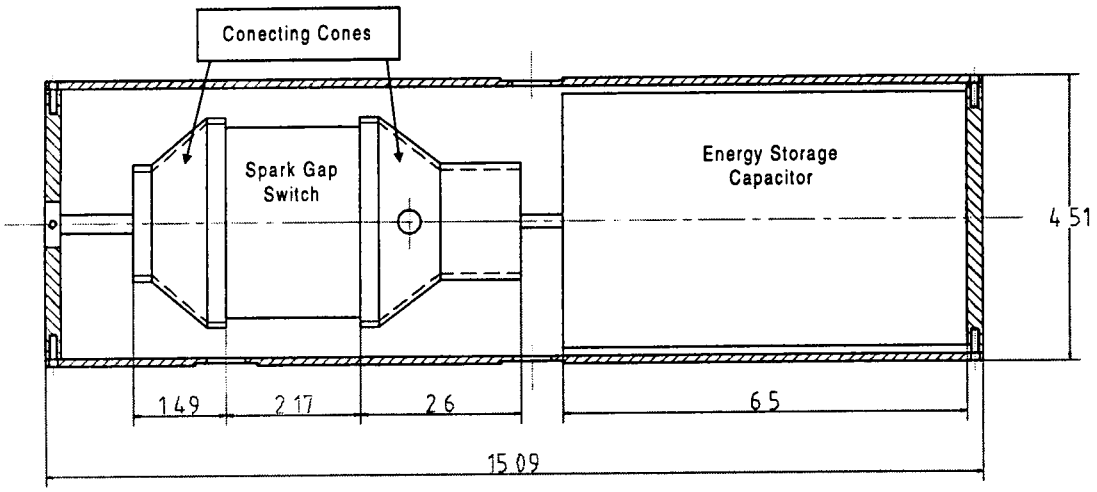

Figure 2.1.1. Schematic of the main energy storage unit.

thruster [13]. From this paper we also took the resistance as an estimate for our device.

The inductance of the cone is given by

$$L_{con} = \int_0^a \frac{dL}{dx} dx = \frac{\mu_0}{2\pi} \int_{x=0}^{x=a} \ln \frac{R}{r_{con0} - bx} dx \qquad [2.1.1]$$

with

R: radius of the pipe (0.1082 m)

r_{con0}: large radius of cone (0.0762m)

a: length of the cone (0.0889 m)

b: slope of the cone

μ_0: permeability of free space ($4\pi \times 10^{-7}$ henry/ m).

After solving the integral the inductance for the conical regions of the pipe is given by

$$L_{con} = \int_0^a \frac{dL}{dx} dx = \frac{\mu_0}{2\pi}\left[a \ln R + \frac{a}{r_{con0} - r_{cone}}\left(\ln \frac{(r_{cone})^{r_{cone}}}{(r_{con0})^{r_{con0}}} + r_{con0} - r_{cone} \right)\right]. \qquad [2.1.2]$$

with

r_{cone}: small radius of the cone (0.0254 m).

The inductance for the coaxial parts like the capacitor and the switch is given by,

$$L_i = \frac{\mu_0}{2\pi} l_i \ln \frac{R}{r_i}. \qquad [2.1.3]$$

with

i: values for the switch (S) and capacitor (C)

r_C: radius of the capacitor (0.1016 m)

r_S: radius of the switch (0.0508 m)

l_C: length of the capacitor (0.17145 m)

l_S: length of the switch (0.076 m).

The entire inductance for the pipe is then approximately given by

$$L = L_C + 2L_{con} + L_S. \qquad [2.1.4]$$

The pipe inductance was 42.1 nH. Additionally, we also had to consider the inductance of the capacitor itself, the switch inductance, and the inductance of the cables and the thruster.

RLC circuit

The basic equations for a RLC circuit can be derived from Kirchhoff's voltage law. Kirchhoff's voltage law is given by [14]

$$L\frac{di}{dt}+Ri+\frac{1}{C}\int idt = LC\frac{d^2v}{dt^2}+RC\frac{dv}{dt}+v=e_s(t) \qquad [2.1.5]$$

with

$$i=C\frac{dv}{dt}. \qquad [2.1.6]$$

After the capacitor is charged, there is no external energy source involved and $e_s(t)$ can be set to 0, resulting in a simple series RLC circuit. By solving the differential equations we get the equations for the voltage in time v(t), the current in time i(t) and the charge in time q(t), which describe the discharge behavior of an optimal power circuit.

The charge is given by

$$q(t)=CV_0\sqrt{1+\frac{\alpha^2}{\omega_d^2}}e^{(-\alpha t)}\cos(\omega_d t-\phi). \qquad [2.1.7]$$

The voltage of the capacitor is given by

$$v(t)=\frac{q(t)}{C} \qquad [2.1.8]$$

and the current is given by

$$i(t)=-V_0\sqrt{\frac{C}{L}}\frac{\omega_n}{\omega_d}e^{(-\alpha t)}\sin(\omega_d t) \qquad [2.1.9]$$

with

$$\omega_n = \frac{1}{\sqrt{LC}} \qquad [2.1.10]$$

$$\omega_d = \sqrt{\omega_n^2 - \alpha^2} \qquad [2.1.11]$$

$$\alpha = \frac{R}{2L} \qquad [2.1.12]$$

$$\tan\phi = \frac{\alpha}{\omega_d}. \qquad [2.1.13]$$

LR circuit

By using Kirchhoff's voltage law for the LR circuit we obtain the following expression for the current [14]:

$$i(t) = I_0 e^{-Rt/L} \qquad [2.1.14]$$

with I_0 being the maximum current of the RLC circuit from equation [2.1.9].

2.2 ELECTROMAGNETIC/ ELECTROTHERMAL ACCELERATION

Most of the pulsed plasma thrusters (PPT) are optimized for the use of electromagnetic acceleration of the plasma. This results in a specific impulse of approximately 1000s to 1400s with an efficiency of 6% to 11%. Today, the thermal

thrusters like arcjets are much more efficient than the PPT's in the same range of specific impulse. The paper "Electromagnetic Acceleration in Pulsed Plasma Thrusters" written by D. Keefer and R. Rhodes [12] leads to the conclusion that a larger part of the acceleration of the plasma is provided by electrothermal processes, mainly ohmic heating of the plasma from the arc itself, and the plasma is accelerated by thermal expansion in the nozzle. The analysis of the electromagnetic performance used concepts developed for a plasma armature railgun [12, 15]. In order to give an example for the efficiency expectations for an electromagnetic accelerator, values of present PPT configurations were taken [13]. With these values a specific impulse of 435 s and a thrust efficiency of approximately 1.2% could be estimated [12]. It should be mentioned that the results above represent the maximum values and in reality the values would be smaller [12].

The measured performance parameters of this thruster gave significantly higher values with a specific impulse of 960 s and a thrust efficiency of 5.9% [12]. This led to the suggestion that the main part of the acceleration of the plasma was provided by electrothermal acceleration rather than by electromagnetic acceleration. Our experiments strongly supported this hypothesis as can be seen in Chapter 4.

To support the above stated hypothesis, a thermal coaxial pulsed plasma thruster was designed to investigate the thruster performance due to electrothermal acceleration with negligible electromagnetic acceleration. This section provides the basic equations that were used in the analysis of the experimental data.

The maximum force (F(t)) exerted on the propellant can be written as,

$$F(t) = \dot{m} v_{ex} \qquad [2.2.1]$$

with

$\dot{m}$: mass flux

v_{ex}: exhaust velocity

With the equation above the total impulse for a single shot, the so called impulse bit (I_b) is given by

$$I_b = \int_0^{\tau} F(t) dt \qquad [2.2.2]$$

with τ being the total pulse time.

As we measured the mass ablation per shot (m) and the exhaust velocity (v_{ex}) we were interested in an expression for the impulse bit calculated with the recorded experimental data. Therefore the total impulse was written in terms of ejected propellant per shot (m_{sh}) and the exhaust velocity,

$$I_b = m_{sh} v_{ex} . \qquad [2.2.3]$$

With the expression for the specific impulse,

$$I_{sp} = v_{ex}/g \qquad [2.2.4]$$

solved for the velocity we obtained the equation for the impulse bit in terms of specific impulse,

$$I_b = m_{sh} I_{sp} g. \qquad [2.2.5]$$

To estimate the thrust efficiency (η_T), which was defined by the ratio of the thrust kinetic energy (E_T) to the initial stored energy (E_0),

$$\eta_T = \frac{E_T}{E_0} \qquad [2.2.6]$$

the thrust kinetic energy for a single impulse was calculated with

$$E_T = \frac{1}{2} m_{sh} v_{ex}^2 = \frac{1}{2} m_{sh} (I_{sp} g)^2 = \frac{1}{2} I_b (I_{sp} g). \qquad [2.2.7]$$

In our case we used the first expression of equation [2.2.7] as we measured the mass ablation per shot and the exhaust velocity in the experiments. To estimate the expected pulse efficiency with the electric parameters of our power circuit we used the equations for an underdamped RLC circuit, as mentioned in Section 2.1. With the simplifying assumption that $\omega_d = \omega_n$ in equation [2.1.9] we obtain an approximate expression for the current as

$$i(t) = V_0 \sqrt{C/L}\, e^{-\frac{Rt}{2L}} \sin\left(t/\sqrt{LC}\right) \qquad [2.2.8]$$

where

V_0: initial voltage on the energy storage capacitor

C: capacitance of the energy storage capacitor

L: inductance of the power circuit

R: total circuit resistance.

We assumed further, since we were interested in a best case estimate, that all the energy dissipated to accelerate the plasma was exerted in the first positive cycle of the damped sinusoid. This meant that $Rt/2L << 1$ with

$$t = \tau = \pi\sqrt{LC}\,. \qquad [2.2.9]$$

This was close to our experimental case since we used a crowbar switch to keep the voltage from becoming negative to prevent the capacitor from current reversals and negative charging. With the assumptions above we get the following expression for the current:

$$i(t) \cong V_0 \sqrt{C/L} \sin\left(t/\sqrt{LC}\right). \qquad [2.2.10]$$

This gave us an expression for the initial stored energy,

$$E_0 = \frac{1}{2} C V_0^2. \qquad [2.2.11]$$

We found in the experiments that the mass ablated per shot is directly proportional to the initial stored energy, so that the mass ablated per shot can be given as

$$m_{sh} \propto \alpha E_0. \qquad [2.2.12]$$

We assume that in an ideal case all the ablated mass would be accelerated to the same velocity.

We also can make an estimate for the electrothermal acceleration of a PPT. The derivation of the exhaust velocity can be approached in two ways. First we derive the expression for the exhaust velocity with regard to the enthalpy of the ablated propellant. By using equation [2.2.12] this leads to an expression for the enthalpy (h) given by

$$h = \frac{\eta_H}{\alpha}. \qquad [2.2.13]$$

The factor η_H is an efficiency that relates the initial stored energy and the actual dissipated energy into the propellant. This factor accounts for radiation losses and ohmic heating in the power circuit.

The exhaust velocity is directly proportional to the enthalpy, which gives us the relation for the exhaust velocity,

$$\frac{1}{2}v_{ex}^{\ 2} = \eta_F h. \qquad [2.2.14]$$

The efficiency factor η_F accounts for viscous and frozen flow losses and represents the flow efficiency. Substituting the enthalpy from equation [2.2.13] in equation [2.2.14] and using again equation [2.2.12] the exhaust velocity is given by

$$v_{ex} = \sqrt{2\eta_H \eta_F E_0 / m_{sh}}\,. \qquad [2.2.15]$$

This shows that the exhaust velocity is directly proportional to the initial stored energy and inversely proportional to the ablated mass. The behavior of the exhaust velocity with different propellants (different mean molecular weights) is of great interest, because we are looking at electrothermal processes.

The equation for the effective exit velocity of a gaseous propellant for thermal expansion in a normal expansion nozzle is [7]

$$v_e = w_e + \frac{A_E}{\dot{m}}(p_E - p_a), \qquad [2.2.16]$$

with

v_e: effective exit velocity

w_e: exit velocity

A_E: exit area

$\dot{m}$: mass flux

p_E: nozzle exit pressure

p_a: environmental pressure.

If we assume expansion into vacuum ($p_a = 0$) we obtain en expression for the exit velocity (w_e),

$$w_e = \sqrt{2(h_0 - h_E)} = \sqrt{2c_p(T_0 - T_E)} \qquad [2.2.17]$$

with

h_0: stagnation enthalpy

h_E: enthalpy at nozzle exit

T_0: stagnation temperature

T_E: temperature at nozzle exit

c_p: specific heat at constant pressure.

With the assumption that $T_E = 0$ at expansion into vacuum this leads to an expression for the exhaust velocity given by

$$v_{ex} = \sqrt{\frac{2\gamma}{\gamma - 1}\frac{RT_0}{M_{mean}}} \qquad [2.2.18]$$

with

$$\gamma = \frac{c_p}{c_v} \qquad [2.2.19]$$

where

c_v: specific heat at constant volume.

For a solid propellant we then find that the exhaust velocity is directly proportional to the plasma temperature T_0 and inversely proportional to the mean molecular weight M_{mean} of the propellant,

$$v_{ex} \propto \sqrt{\frac{T_0}{M_{mean}}}. \qquad [2.2.20]$$

This relation shows, that propellants with a lower mean molecular weight should give better performance in PPTs. This can also be seen from the experimental results in Chapter 4.

If we again consider an ideal case with η_H and η_F being unity we can calculate, for the values stated before, a specific impulse of 3964 s which is significantly higher than the specific impulse we obtained from pure electromagnetic acceleration. This shows again that electrothermal acceleration is the most important acceleration mechanism in such thrusters.

2.3 ELECTRON NUMBER DENSITY

With our interferometer we were measuring the change in index of refraction produced by the electrons in the moving plasma. It was therefore of interest to estimate the electron number density in the plasma. We derived a simple equation for the electron number density as a function of phase shift and effective path length. Figure 2.3.1 shows the paths of the reference and measurement beam with significant values.

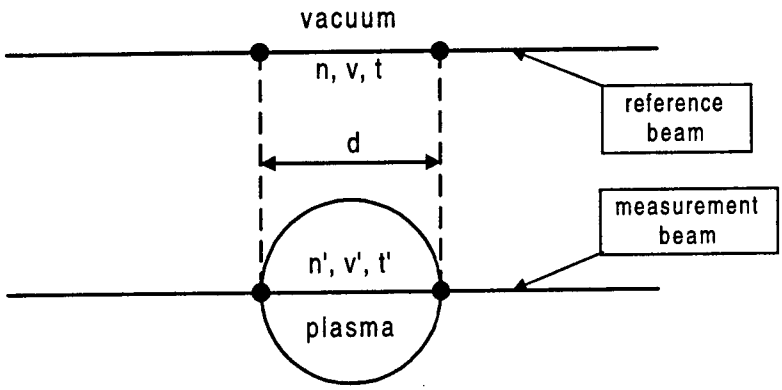

Figure 2.3.1. Schematic of the paths of the reference and measurement beams with d as the effective path length which is the same for both beams, n, n' index of refraction for vacuum and plasma respectively, v, v' phase velocities of the laser in vacuum and plasma respectively and t, t' time to cross the effective path length in vacuum and in plasma respectively.

For the measurement of the change in index of refraction from vacuum to the plasma the values marked with a prime characterize the values of the plasma and the values without any special mark characterize the values of the vacuum. The time the laser needs to cross the same effective path length for both mediums is different due to the different optical densities of vacuum compared to the plasma.

The time the laser needs to cross the same path length in the two different mediums can be written as,

$$t = \frac{d}{v} \qquad [2.3.1]$$

$$t' = \frac{d}{v'}. \qquad [2.3.2]$$

with

v, v': phase velocities of laser beam

t, t': time for the beam to cross the effective path length

d: effective path length.

The phase velocities can be written as [16],

$$v = \frac{c}{n} \qquad [2.3.3]$$

$$v' = \frac{c}{n'} \qquad [2.3.4]$$

with

c: velocity of light (3×10^8 m/s)

n, n': index of refraction.

With equations [2.3.1] to [2.3.4] we find an expression for the time difference between the case of vacuum and the case of the plasma,

$$\Delta t = t - t' = \frac{d}{c}(n - n'). \qquad [2.3.5]$$

The time for a 2π phase shift is given by,

$$t_0 = \frac{1}{f}. \qquad [2.3.6]$$

with

f: laser frequency [1/s]

With equations [2.3.5] and [2.3.6] we obtain an expression for the phase shift, which was measured during the experiments,

$$\Delta\varphi = \frac{2\pi\Delta t}{t_0} = 2\pi f \frac{d}{c}(n - n'). \qquad [2.3.7]$$

The expression for the index of refraction was taken from source [16],

$$n' = \sqrt{1 - \frac{\Pi^2}{\omega^2}}. \qquad [2.3.8]$$

With a Taylor expansion around (Π^2/ω^2) and neglecting of the higher order terms, which was appropriate, as they were very small, we could write equation [2.3.8] as

$$n' = 1 - \frac{1}{2}\frac{\Pi^2}{\omega^2}. \qquad [2.3.9]$$

where ω is given by

$$\omega = 2\pi f \qquad [2.3.10]$$

with

ω: laser frequency [radians/s]

The plasma frequency Π_- [rad/s] was also taken from source [16] and is given by

$$\Pi_- = \sqrt{\frac{Ne^2}{m_-\varepsilon_0}} \qquad (N - cm^{-3}) \qquad [2.3.11]$$

with

N: electron number density

e: charge of an electron (1.6×10^{-19} coul)

m_-: electron mass (9.1×10^{-31} kg)

ε_0: permittivity of free space (8.85×10^{-12} farad/m).

Using the equations [2.3.7], [2.3.9], [2.3.10] and [2.3.11] and assuming that n = 1 for vacuum the phase shift is given by

$$\Delta\varphi = d\frac{8.1e7 * \pi}{fc}N\,. \qquad [2.3.12]$$

If we solve equation [2.3.12] for the electron number density N we obtain the expression for the electron number density as a function of phase shift and effective path length:

$$N = \frac{fc}{8.1e7 * \pi}\frac{\Delta\varphi}{d} = 5.59e20\frac{\Delta\varphi}{d} \qquad [m^{-3}] \qquad [2.3.13]$$

where the frequency of the laser can be written as

$$f = \frac{c}{\lambda} \qquad [2.3.14]$$

with

$\lambda = 633 \times 10^{-9}$ m (wavelength of the laser).

CHAPTER 3

EXPERIMENTS

3.1 EXPERIMENTAL SETUP

The theoretical background for the experimental research work of this thesis was described in the previous chapter. In order to investigate the theory that thermal acceleration plays a major part in the overall performance of electric thrusters like the coaxial thruster, an experiment for some basic research on a pulsed plasma thruster was designed. With this experiment the first steps to gain understanding of the influence of nozzle design and propellant on the overall performance of such a thruster were taken.

Figure 3.1.1 shows a schematic of the experimental setup. The main parts are described in detail in the following sections of this chapter. First of all the thruster itself had to be designed, which is described in detail in Section 3.2.

A vacuum chamber was built to accommodate the thruster testing. The main part of the vacuum chamber consisted of a cross-shaped glass pipe of inner diameter 15.2 cm. The length of each section was approximately 38 cm. The chamber was connected through glass pipes to a roughing pump in conjunction with an oil diffusion pump, which allowed the chamber to be evacuated to background pressures down to

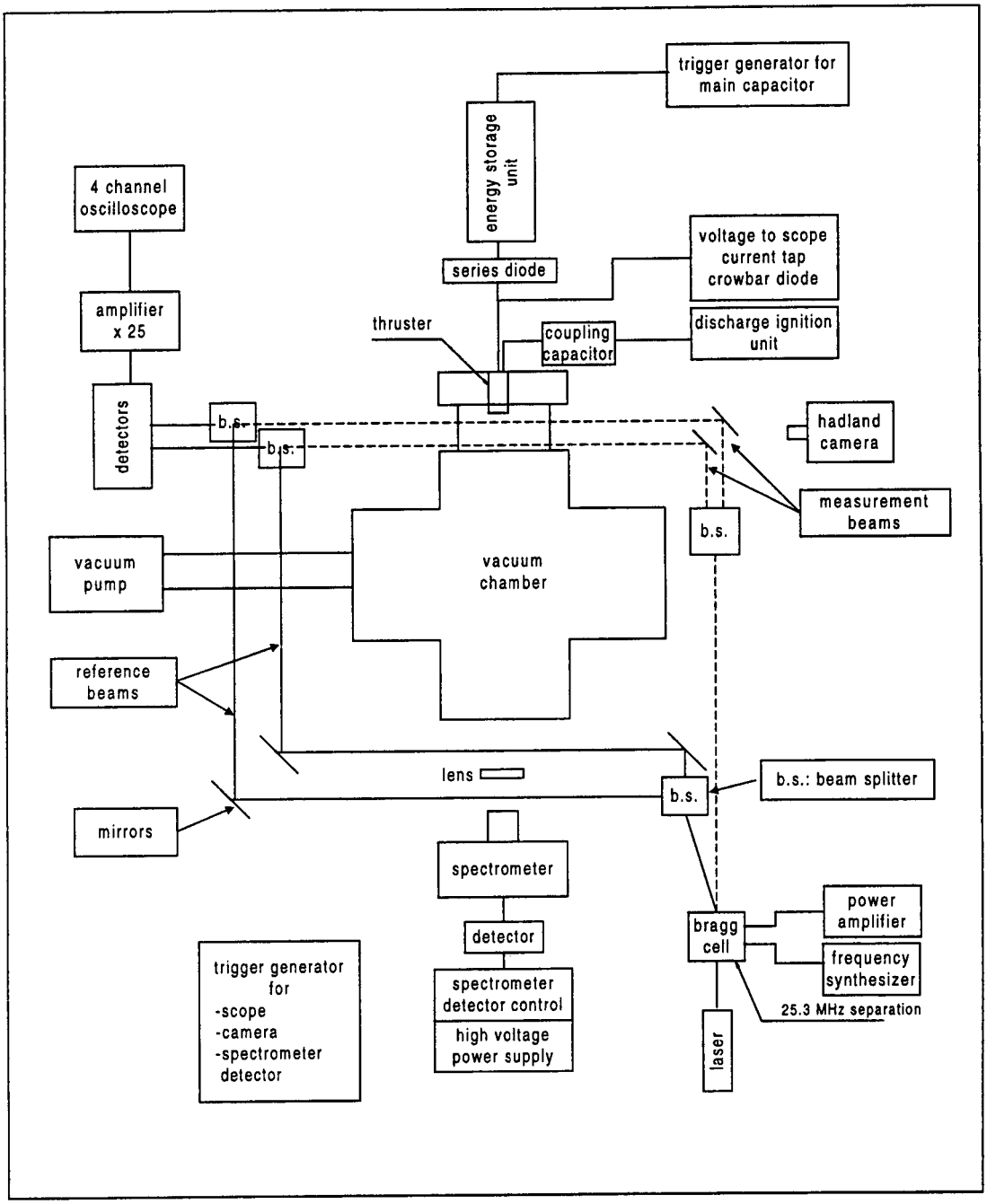

Figure 3.1.1. Schematic of the experimental setup.

10^{-6} Torr. To monitor the pressure a thermocouple gauge and an ionization gauge were available.

The thruster was mounted at one end of the chamber. The exit of the nozzle was located in a squared part of the vacuum chamber connected over flanges. The walls of the squared part were approximately 15 cm by 7 cm and also made of glass. This section allowed us to make measurements of the exhaust plume. Velocity measurements were made with a high-speed camera and a dual beam laser interferometer that passed through the squared part of the vacuum chamber. Detailed descriptions of this equipment are given in the sections below.

A Le Croy 9314 four-channel oscilloscope with 100 mega samples/sec for each channel was used to collect phase shift data from the interferometer and the current and voltage data. The current and voltage data were taken directly after the main capacitor, so that the current and voltage supplied to the thruster were directly measured.

At the opposite side of the thruster flange a spectrometer was set up and focused through a lens to look directly into the nozzle and the exiting plasma. The power to run the thruster was obtained from a high voltage power supply. This high voltage power supply was connected to the energy storage capacitor, which is also described in detail later. Several trigger generators and triggers were used to set the timing for all the devices.

3.2 THRUSTER

The thruster itself is a very simple design. The nozzle consists of mainly three parts, the cathode made of copper, which is the outer electrode, the plastic propellant, and the center conductor anode made of tungsten. The propellant is also used as insulation against voltage breakdowns at places other than the nozzle exit. We used two different nozzle sizes, one with a ½ in (1.27 cm) nozzle exit diameter and one with a ¾ in (1.905 cm) nozzle exit diameter. The anode was 1/8in (0.3175 cm) in diameter in both cases. The propellant and the cathode formed the nozzle shape, with both parts having walls with 30 degrees half angle.

The breakdown was initiated by creating a sufficiently high voltage potential gradient from the cathode to the anode. No spark plug was used, unlike other already existing thrusters. The exact measurements of the parts and an assembly drawing can be found in figures 3.2.1 and 3.2.2 on the next pages.

When a sufficiently high voltage is supplied, breakdown occurs from the cathode over the propellant to the anode and ablates some of the propellant material. At the very beginning, the breakdown occurs from point to point, but instantly expands over the whole nozzle area. The ablated material creates hot plasma that is then accelerated out the nozzle exit. Figure 3.2.3 shows a schematic of the thruster with the connecting flange to the vacuum chamber and the breakdown path of the ark.

Tungsten Anode

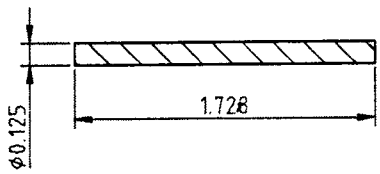

Propellant/ Insulator (Teflon or polyethylene)

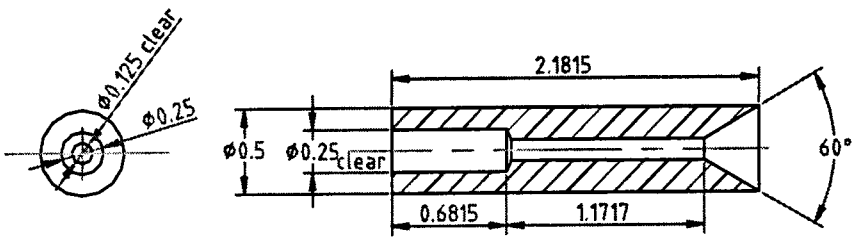

Cathode

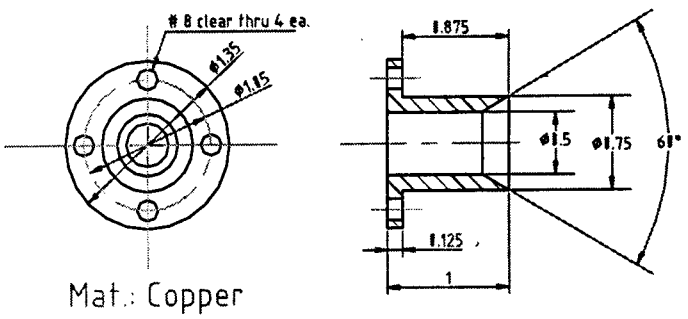

Complete Nozzle

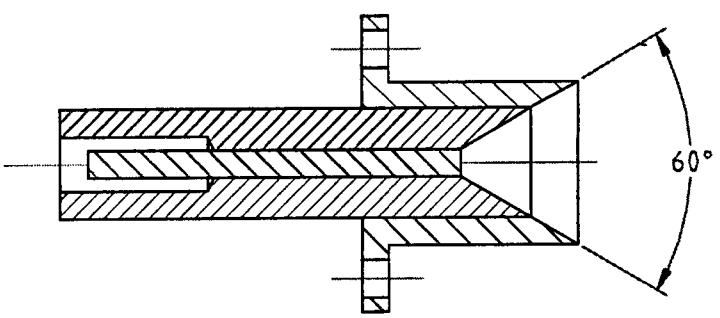

Figure 3.2.1. Drawing set for the ¾ inch (large) nozzle.

Tungsten Anode

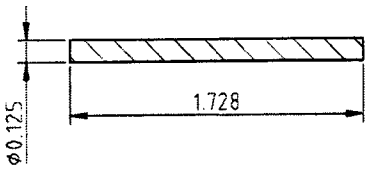

Propellant/ Insulator (Teflon or polyethylene)

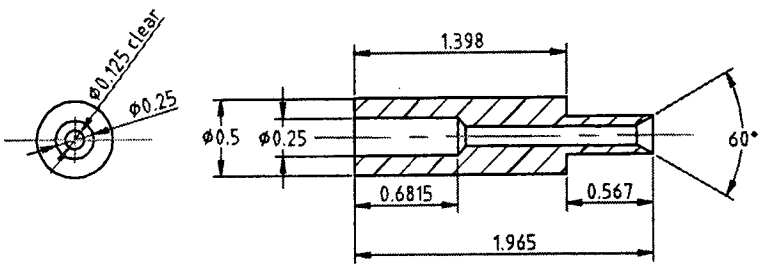

Cathode

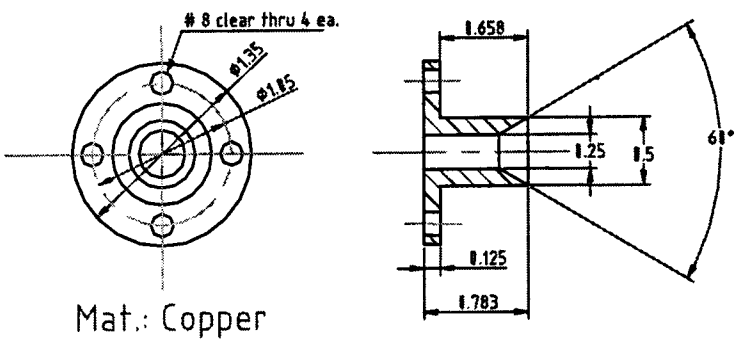

Complete Nozzle

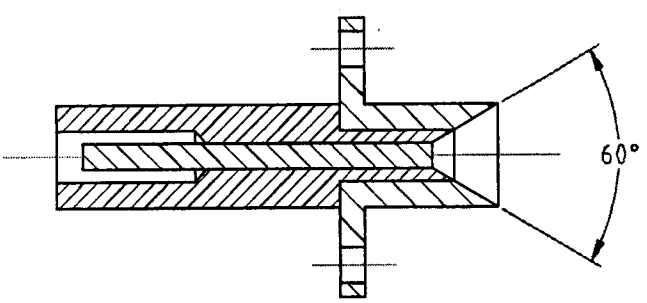

Figure 3.2.2. Drawing set for the ½ inch (small) nozzle.

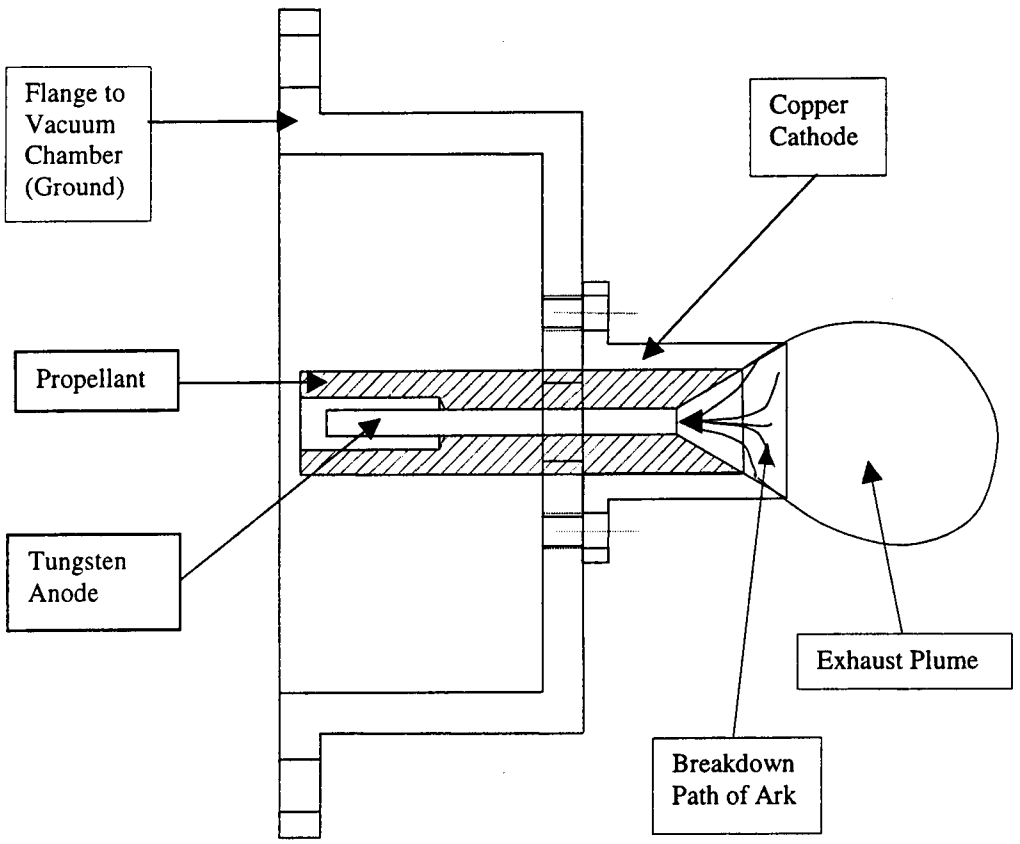

Figure 3.2.3. Breakdown path of the arc from the cathode to the anode.

3.3 POWER SUPPLY

High Voltage Power Supply

A Spellman SL 150 power supply was used to charge the main energy storage capacitor to the desired operating voltages. Its charging rate is 5 mA up to 30 kV. We used a charging rate of 4 mA and charged the capacitor to voltage levels from 7 kV to 11 kV for the different tests.

Ignition Circuit

The main parts of the ignition circuit were the power supply with the energy storage capacitor and the spark gap switch, the discharge ignition unit with a coupling capacitor, a crowbar diode and a series diode.

The **crowbar diode** shorts out reverse current flows into the energy storage power supply to prevent voltage reversal in the main capacitor and lengthen the spark gap switch lifetime by suppressing ringing in the switch.

The **discharge ignition unit** with the coupling capacitor parallel to the main capacitor was necessary to raise the voltage potential of the anode to enable breakdown without using a spark plug, which would have complicated the design of the system. The discharge ignition unit supplied up to an additional 20 kV to the voltage potential gradient between the anode and the cathode to create a glow discharge, and to initiate a breakdown path for the discharge of the main capacitor. The coupling capacitor with a capacitance of 500 pF was used to isolate the low impedance of the ignition unit.

The **series diode** was needed to increase the impedance to the main capacitor so that the breakdown supply could be operated with a second trigger and the current was not absorbed by the main capacitor.

Two Maxwell **energy storage capacitors** one of 3.28 μF and one of 3.29 μF measured capacitance were used during the experiments because the first capacitor failed. Both had a 12 kV voltage rating with a 25 kA maximum peak current rating. The capacitors had a cylindrical metal case, which was 4in (10.2 cm) in diameter and 6.5 in (16.5 cm) long.

An EG&G GP-86 **triggered spark gap switch** was used. The voltage operation range of this switch is 6 kV to 15 kV. The lifetime expectation in crowbar service and with a 25 kA peak at 0.4 coulomb and an E/R of 5000 joules/ohm is 5000 to 20,000 shots. Two of these switches were purchased during the tests, because the lifetime was exceeded. To trigger the switch, another high voltage pulse generator was used with an output of approximately 30 kV. Figure 3.3.1 shows the electrical diagram of the ignition circuit and Figure 3.3.2 shows a schematic of the ignition circuit.

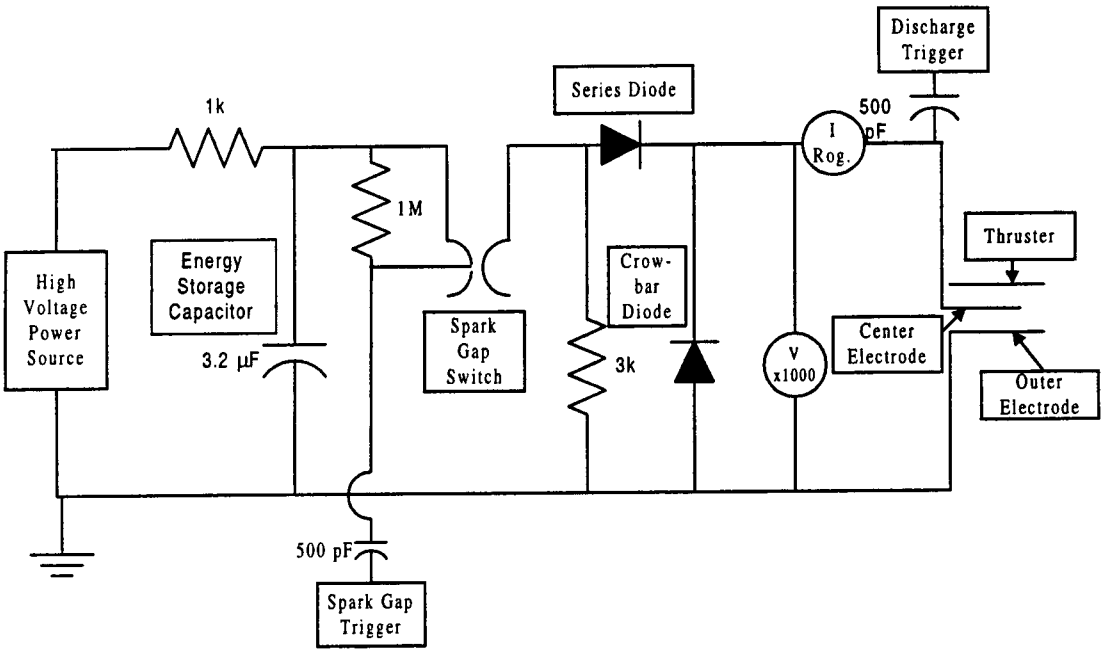

Figure 3.3.1. Diagram of the ignition circuit.

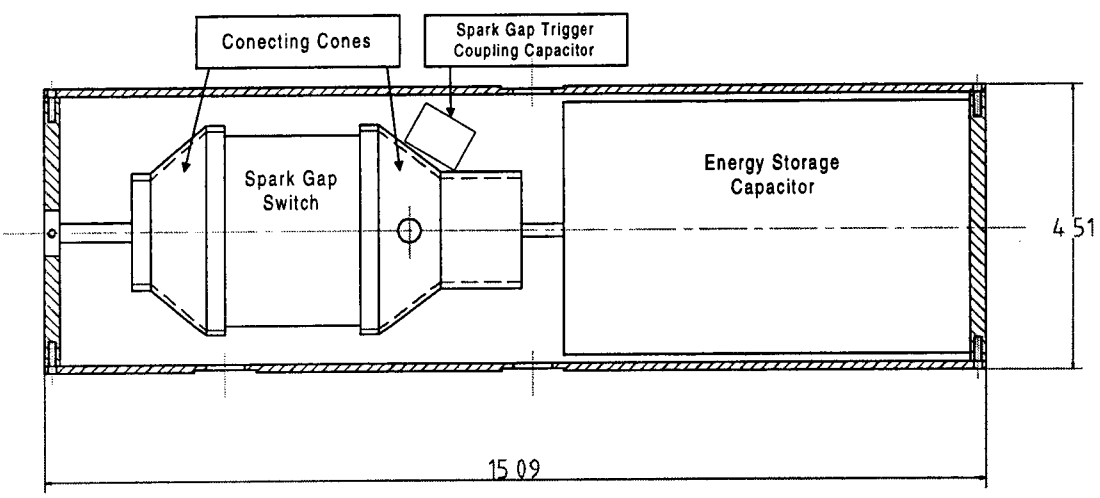

Figure 3.3.2. Schematic of the main ignition unit.

3.4 DATA ACQUISITION EQUIPMENT

Interferometer

A two- beam laser interferometer was designed to measure the exhaust velocity and the electron density. The two beams enabled us to measure the phase shift as the exhaust plume crossed the beams at two different times, and with a known distance between the beams it was possible to calculate the velocity.

The **laser** that was used was a Spectra Physics Mo. 127 60 mW He-Ne-Laser (633 nm). The Laser was aimed towards an **acousto-optic modulator or Bragg cell** in which the beam was split into two beams with a 25.3 MHz frequency difference, which was the peak resonance of the crystal. One beam was used as the reference beam and the other as the measurement beam for heterodyne phase detection. The split of the beam takes place by exciting a crystal, which creates a travelling wave in water that splits the laser beam and two beams of different frequency leave the cell at an angle to each other. A SI-105 Syntest frequency synthesizer was used to supply the frequency for the crystal in combination with an EIN 325LA RF power amplifier (50dB, 250 kHz to 150 MHz).

The **reference beam** was guided into a beam splitter to obtain two beams with the same frequency. These beams were guided over mirrors around the vacuum chamber, without being exposed to the exhaust plume of the thruster.

The **measurement beam** coming from the Bragg cell was also split into two beams with the same frequency, which were guided over mirrors through the square part of the vacuum chamber. The exhaust plume of the thruster crossed the beams,

creating a phase shift. The beams were located 3.81 cm downstream of the nozzle exit, to reduce existing non-plasma sources for phase shift like electric noise coming from the trigger switch, directly after the trigger.

The four beams were then recombined to two beams, one reference with one measurement beam at a time. The resulting two beams included the phase shift information needed to determine the velocity after numerical analysis and were detected by two pin diodes. These signals were amplified by 25x with a SRS SR445 DC-300MHz amplifier and recorded with the oscilloscope mentioned at the beginning of this chapter. Figure 3.4.1 shows the schematic of the interferometer setup with all electronic and optical parts.

Spectrometer

A ¼ m Czerny-Turner by Jarrell-Ash spectrometer was used to perform basic spectral analysis. The spectrometer has a 1200 G/mm grating. The detector was a EG&G Mo.1461 optical multi-channel analyzer. It works with an intensified diode array of 700 points which corresponds to a resolution of approximately 0.7 Å per unit.

Camera

A Hadland IMACON 790 camera was used to take pictures of the exhaust plume. Most of the pictures were taken with an interframe time of 1 μs. The velocity could be calculated using the time difference between the pictures and the travel distance of the exhaust plume measured from the pictures.

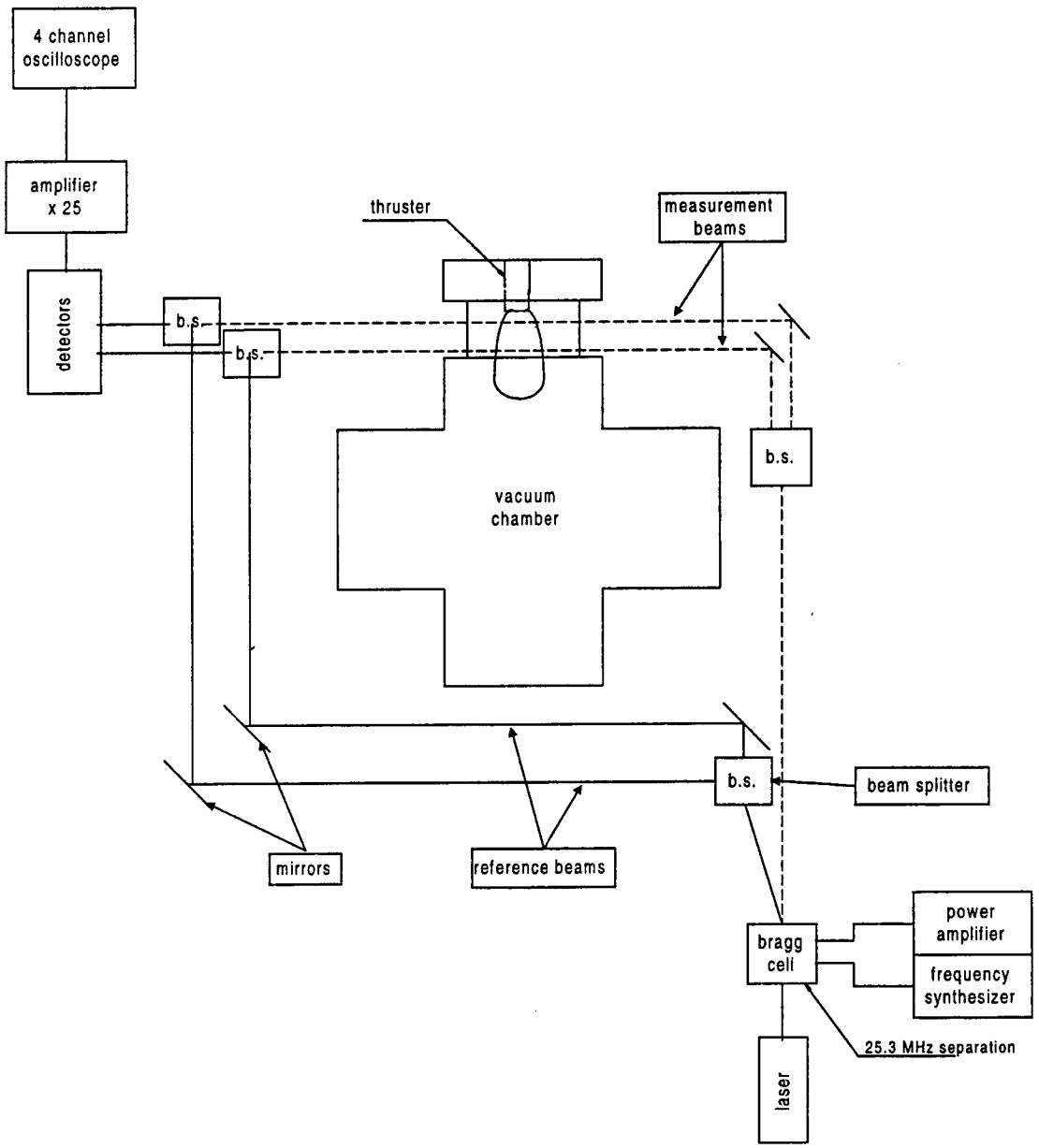

Figure 3.4.1. Schematic of the interferometer setup.

Timing

To operate the experiment and time all the equipment so the data could be taken as wanted, we used two trigger generators and two high power voltage pulse generators. The first trigger generator was a Hadland Photonics three channel pulse delay generator. Channel one and three were used to create a loop to run the experiment automatically for a specified number of shots. Channel one was used for the start of the overall experiment timing and channel three was used to give a delay of 15 s between each trigger. These 15 s intervals were used to recharge the high voltage capacitor. Channel one fed the discharge trigger and the second delay generator. Channel two was used to trigger the camera and had a voltage output of 50 V.

An EG&G Model 9650 four channel digital delay generator was the second trigger generator used. The first channel was connected to channel two of the Hadland generator. Channel two fed the spectrometer and the oscilloscope. Channel three was connected to the spark gap trigger generator and triggered 1 ms before the others.

All triggers were conventional TTL triggers except the triggers for the camera, the spark gap switch and the breakdown capacitor. The trigger for the spark gap switch was locally fabricated and had an output of 30 kV with a pulse width of ½ μs. The discharge trigger for the discharge ignition unit had an output of 20 kV and a pulse width of 2 ms provided by a race car high energy ignition system. A pulse width of approximately 2 ms was necessary to enable a large enough glow discharge in the nozzle to establish the main arc.

Scale

A Sartotius 1712 MP8 scale was used with a measure range of 30mg or 60 mg and a accuracy of 0.01 mg or 0.1 mg respectively. For the weighing of the propellant the 30 mg / 0.01 mg range was used.

Remarks

Several problems appeared during the design of the experiment that are worth mentioning to help other experimentalists at their future work.

The first problem that occurred was that several of the connections between the thruster and the energy storage capacitor broke although rated for these kinds of voltages and currents. This can be explained by the very short rise times for the current during the breakdown in the nozzle. As no other connectors were available, the use of connectors were minimized as much as possible and the different devices were connected directly. Also, the insulation at several locations had to be improved.

Another big problem was the electric noise mainly coming from the trigger switch. This noise also created phase shifts in the interferometer, so that nearly no useful signals could be recorded during the trigger and crowbar events. This was improved by several grounding wires and a Faraday cage over the detecting diodes. At the same time, the interferometer beams were moved downstream, to give the noise time to fade out before the actual data was recorded. Also to reduce the influence of light noise in the interferometer signal, a narrow band pass light filter was used.

It appeared that the ratings of the energy storage capacitor were not totally appropriate for our application. A capacitor with a much higher voltage rating like 30 kV or higher would have been useful to be able to run the experiment without a discharge ignition unit. We found out that we could not get reliable breakdown at the low pressures that were available. But even with the ignition unit we had to run the experiment at a background pressure of approximately 30 mTorr for the small nozzle and approximately 100 mTorr for the big nozzle to be able to get breakdown. So the better choice if one wants to have the same stored energy level would be to have a capacitor of smaller capacity, but much higher voltage rating.

CHAPTER 4

ANALYSIS AND RESULTS

The purpose of this research experiment was to obtain some basic performance data such as mass ablation per shot (m_{sh}) and exhaust velocities (v_{ex}) for a coaxial PPT. We recorded the current (I) and voltage (V) input to the thruster. From the measured exhaust velocities and the mass ablation several other thruster performance parameters were estimated such as specific impulse (I_{sp}), impulse bit (I_{bit}), the thrust efficiency (η_T) and others. Spectra of the exhaust plume were also taken to distinguish the species in the plasma.

To investigate the influence of nozzle size, propellant and power level on thruster performance, experiments were run with two different nozzle sizes and two different propellants at several initial stored energy levels (E_0). Table 4.1 shows the data taken with the different experimental configurations. The slightly different energy levels shown in the table result from the use of two different capacitors as already mentioned in the description of the experimental setup.

Table 4.1. Listing of experimental configurations with measured parameters.

½ inch Nozzle				¾ inch Nozzle			
Teflon		**Polyethylene**		**Teflon**		**Polyethylene**	
E_0 [J]	**Data**	**E_0 [J]**	**Data**	**E_0 [J]**	**Data**	**E_0 [J]**	**Data**
80.6 (7 kV)	v_{ex}, m_{sh}, I, V, spectro	80.6 (7 kV)	v_{ex}, m_{sh}, I, V, spectro	80.4 (7 kV)	v_{ex}, m_{sh}, I, V, spectro	80.4 (7 kV)	v_{ex}, m_{sh}, I, V, spectro
105.3 (8 kV)	v_{ex}, I, V, spectro	105.3 (8 kV)	v_{ex}, I, V, spectro	105.0 (8 kV)	v_{ex}, I, V, spectro	105.0 (8 kV)	v_{ex}, I, V, spectro
148.5 (9.5 kV)	v_{ex}, m_{sh}, I, V, spectro	132.8 (9 kV)	v_{ex}, m_{sh}, I, V, spectro	132.8 (9 kV)	v_{ex}, m_{sh}, I, V, spectro	132.8 (9 kV)	v_{ex}, m_{sh}, I, V, spectro
164.5 (10 kV)	v_{ex}, I, V, spectro	164.0 (10 kV)	v_{ex}, I, V, spectro	164.0 (10 kV)	v_{ex}, I, V, spectro	164.0 (10 kV)	v_{ex}, I, V, spectro
199.0 (11 kV)	v_{ex}, m_{sh}, I, V, spectro	198.4 (11 kV)	v_{ex}, m_{sh}, I, V, spectro	198.4 (11 kV)	v_{ex}, m_{sh}, I, V, spectro	198.4 (11 kV)	v_{ex}, m_{sh}, I, V, spectro

4.1 MASS ABLATION

We assume, that the ablated mass per shot is directly proportional to the initial stored energy:

$$m = \alpha E_0$$

with α being a proportionality factor for each configuration. Figure 4.1.1 shows the mass ablated per shot as a function of the initial stored energy for the different tested configurations. From Figure 4.1.1 one can see that for the tested energy levels using polyethylene the increase of ablated material with initial stored energy is approximately linear for both nozzle sizes. One can also see that if the curves for polyethylene were extrapolated to zero energy, they would not cross at zero mass.

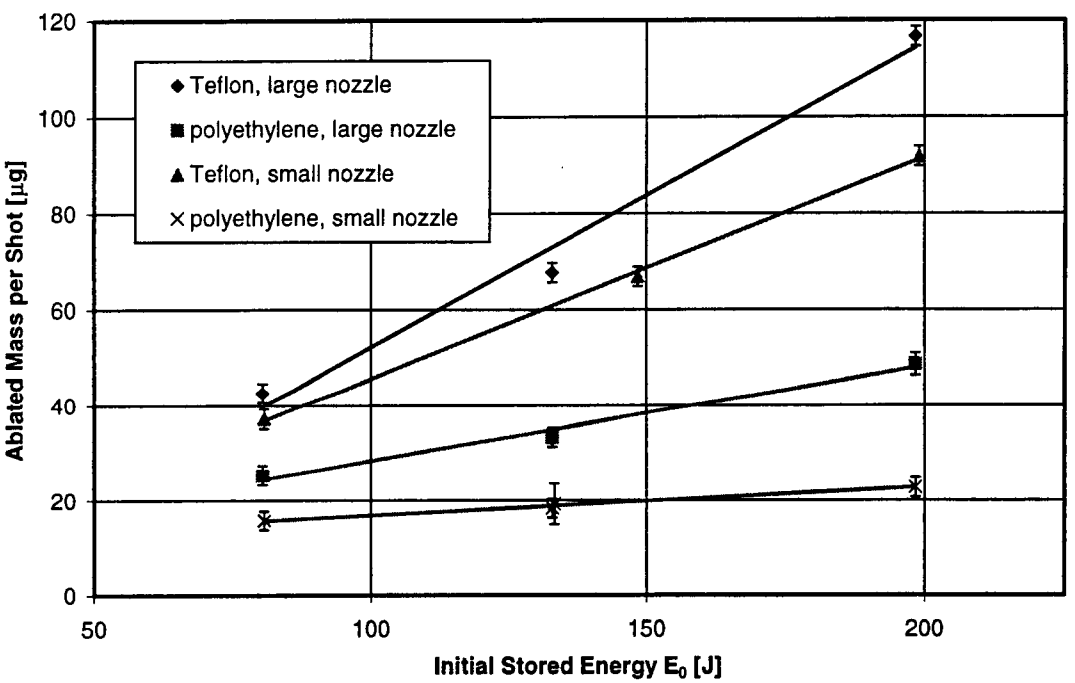

Figure 4.1.1. Measured mass ablation per shot as a function of initial stored energy.

This might be explained by a soot layer, which occurred mainly in the experiments with polyethylene.

We observed during the experiments that a thicker soot layer occurred in the test with polyethylene than with Teflon. The soot, consisting mainly of carbon particles, created a vapor shield, which kept the energy from reaching the surface and ablating more material. The smaller soot layer with Teflon can be explained as free carbon particles and Fluorine combine into a gaseous compound much more easy than carbon and hydrogen, producing fewer free carbon particles.

The cleaner operation of Teflon is one reason why it has been used more often in applications than polyethylene. A disadvantage, on the other hand, is that most of the time more Teflon propellant is ablated than is actually wanted. The vapor shielding is an advantage of polyethylene as a propellant, as less material is ablated leading to a lower propellant consumption. On the other hand there is a possibility that the carbon layer could short out the thruster. This did not occur at our experiments, as the thruster was self-cleaning.

Since less energy is used to ablate material using polyethylene, more energy is available to accelerate the plasma. Polyethylene also has a lower molecular weight and we measured substantially higher exhaust velocities and higher specific impulses with polyethylene.

Teflon ablation in the small nozzle also shows a linear behavior within the measured energy range. The linear fit for the large nozzle with Teflon is not as accurate as the other configurations and might be a result of some misfires at the 198 J

energy level. Another possibility would be that the mass ablation behavior in the big nozzle for Teflon changes at high power levels from linear to non-linear behavior. An explanation for this might be found in the radiation behavior or the pressure and temperature distribution and needs further investigation. Extrapolation of the Teflon curves to zero energy gives approximately zero mass ablation and supports the vapor shield theory mentioned above.

From Figure 4.1.1 and the recorded data we can now calculate the approximate average proportionality factor α for each configuration for the tested energy levels:

Small nozzle, Polyethylene: $\alpha = 0.15$ µg/J

Big nozzle, Polyethylene: $\alpha = 0.27$ µg/J

Small nozzle, Teflon: $\alpha = 0.46$ µg/J

Big nozzle Teflon: $\alpha = 0.54$ µg/J.

The different α for the same propellants can be explained by the different nozzle sizes, as the exposed propellant area to the arc is different. Also pressure differences and temperature differences can contribute. We also observed that the ratio of the mass ablation of the big nozzle to the small nozzle is not linear with the surface ratios of the two nozzles. Temperature, radiation and pressure could be the reason for this behavior. The expected mass ablation per shot for the other energy levels were calculated with the equations of the trendlines. Table 4.1.1 shows a summary of the mass ablation data.

Another interesting aspect of the experimental mass ablation data is the energy flux to the material. The energy flux can be derived as follows.

Table 4.1.1. Listing of resulting mass ablation data.

½ inch Nozzle				¾ inch Nozzle			
Teflon		Polyethylene		Teflon		Polyethylene	
E_0 [J]	m_{sh} [μg]	E_0 [J]	m_{sh} [μg]	E_0 [J]	m_{sh} [μg]	E_0 [J]	m_{sh} [μg]
80.6 (7 kV)	37 ± 2.0	80.6 (7 kV)	16 ± 2.0	80.4 (7 kV)	43 ± 2.0	80.4 (7 kV)	25 ± 2.0
105.3 (8 kV)	48 ± 2.0	105.3 (8 kV)	17 ± 2.0	105.0 (8 kV)	55 ± 2.0	105.0 (8 kV)	29 ± 2.0
133.2 (9 kV)	61 ± 2.0	133.2 (9 kV)	19 ± 4.3	132.8 (9 kV)	68± 2.0	132.8 (9 kV)	33 ± 2.0
148.5 (9.5 kV)	67 ± 2.0	132.8 (9 kV)	18 ± 2.0	164.0 (10 kV)	93 ± 2.0	164.0 (10 kV)	41 ± 2.0
164.5 (10 kV)	75± 2.0	164.0 (10 kV)	21± 2.0	198.4 (11 kV)	117± 2.0	198.4 (11 kV)	49 ± 2.3
199.0 (11 kV)	92 ± 2.0	198.4 (11 kV)	23 ± 2.0				

The power necessary to ablate a certain amount of material is

$$P_S = h_{vap}\, dm/dt$$

with

h_{vap} : heat of vaporization

dm/dt: mass flux.

The power supplied to the surface is assumed to be proportional to the initial stored energy,

$$P_S = \varepsilon E_0.$$

If we assume that the absorbed energy is proportional to the blackbody radiation,

$$\Delta E = \varepsilon \cdot \sigma \cdot T^4 \cdot A_{pr} = \Delta m \cdot h_{vap}$$

one gets the equation for the energy flux to the material

$$\frac{\Delta E}{A_{pr}} = \varepsilon \cdot \sigma \cdot T^4 = \frac{\Delta m \cdot h_{vap}}{A_{pr}}$$

with

Teflon: h_{vap} = 2.2 MJ/kg [17]

Polyethylene: h_{vap} = 1 MJ/kg [18]

ε: Emissivity

σ: Boltzmann Konstant

T: Temperature

A_{pr}: Propellant area

Δm: Mass ablated per shot.

Figure 4.1.2 shows the energy flux as a function of initial stored energy. We can see that the energy flux to the surface for polyethylene is smaller than for Teflon. An explanation could be again the vapor shielding of the carbon soot at polyethylene. This explains also that the polyethylene mass ablation curves from Figure 4.1.1 if they were extracted to zero initial stored energy would not cross zero mass ablation and why less mass of polyethylene is ablated per shot compared to Teflon. One can also see that we again have linear behavior of the curves in the measured energy range.

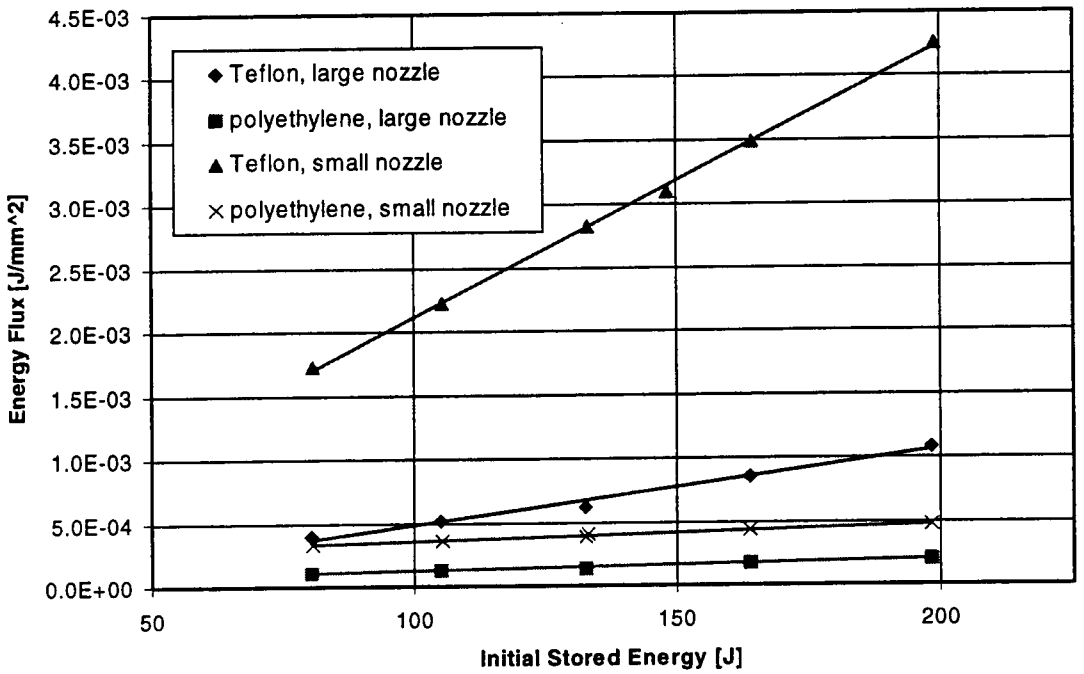

Figure 4.1.2. Energy flux as a function of initial stored energy.

4.2 VELOCITY MEASUREMENTS

The interferometer velocity measurements took place approximately 38 mm down stream of the nozzle exit. The reason it was placed so far away was electric noise as already described in Chapter 3.4. We determined the velocities from the interferometer data by using a phase demodulation and phase correlation program written by Dr. M. Smith from UTSI. The velocities from the pictures were calculated from the moving front of the visible shockwaves. If there were more than two frames available at the same shot to calculate the velocity, all the velocities were calculated and the average was taken. This gave us an average velocity over a certain distance.

We obtained a good correlation within the error bounds between the velocities calculated from the pictures and the velocities from the interferometer data. We could achieve much higher velocities with polyethylene than with Teflon as expected due to the lower mean molecular weight of the polyethylene compared to Teflon. This supported the hypothesis that the acceleration of the propellant is mainly thermal.

We expected to see an increase in velocity with increasing initial stored energy, but this behavior could only be seen with the small nozzle using Teflon and the large nozzle using polyethylene. This might be explained by the increase in mass ablation with increasing energy. More mass was ablated with increasing energy, and so a larger mass had to be accelerated that might have prevented an increase in velocity. Another problem was the increase in electric noise with increasing energy that made the velocity measurements less accurate. The velocities using the large nozzle with polyethylene were so high that they were more difficult to determine due

to the timing of the camera. The velocities at the nozzle exit were also slightly higher than at the point the interferometer measurements took place. The deceleration in the background atmosphere of the vacuum chamber affected polyethylene more than Teflon due to the lower mean molecular weight of polyethylene.

We can see from figure 4.2.1 that the average velocities for the same energy levels with the large nozzle are higher for both polyethylene and Teflon compared to the small nozzle. This suggests that thermal acceleration dominates and shows that the plasma was not fully thermally expanded in the small nozzle. The nozzle size affects the exhaust velocity of polyethylene more than the exhaust velocity of Teflon. This can again be explained by the different mean molecular weights of the two propellants and supports the hypothesis that thermal acceleration dominates for this thruster. There is a significant increase in velocity with increasing energy for polyethylene with the large nozzle. The improvement in exhaust velocity as described above gives polyethylene an advantage over Teflon. Table 4.2.1 shows the measured average velocities for the different configurations.

We assumed that the exhaust velocity (v_{ex}) is related to the mean molecular weight (M_{mean}) of the propellant as follows, assuming that Teflon and polyethylene have the same temperatures:

$$v_{ex} \propto \sqrt{\frac{1}{M_{mean}}}.$$

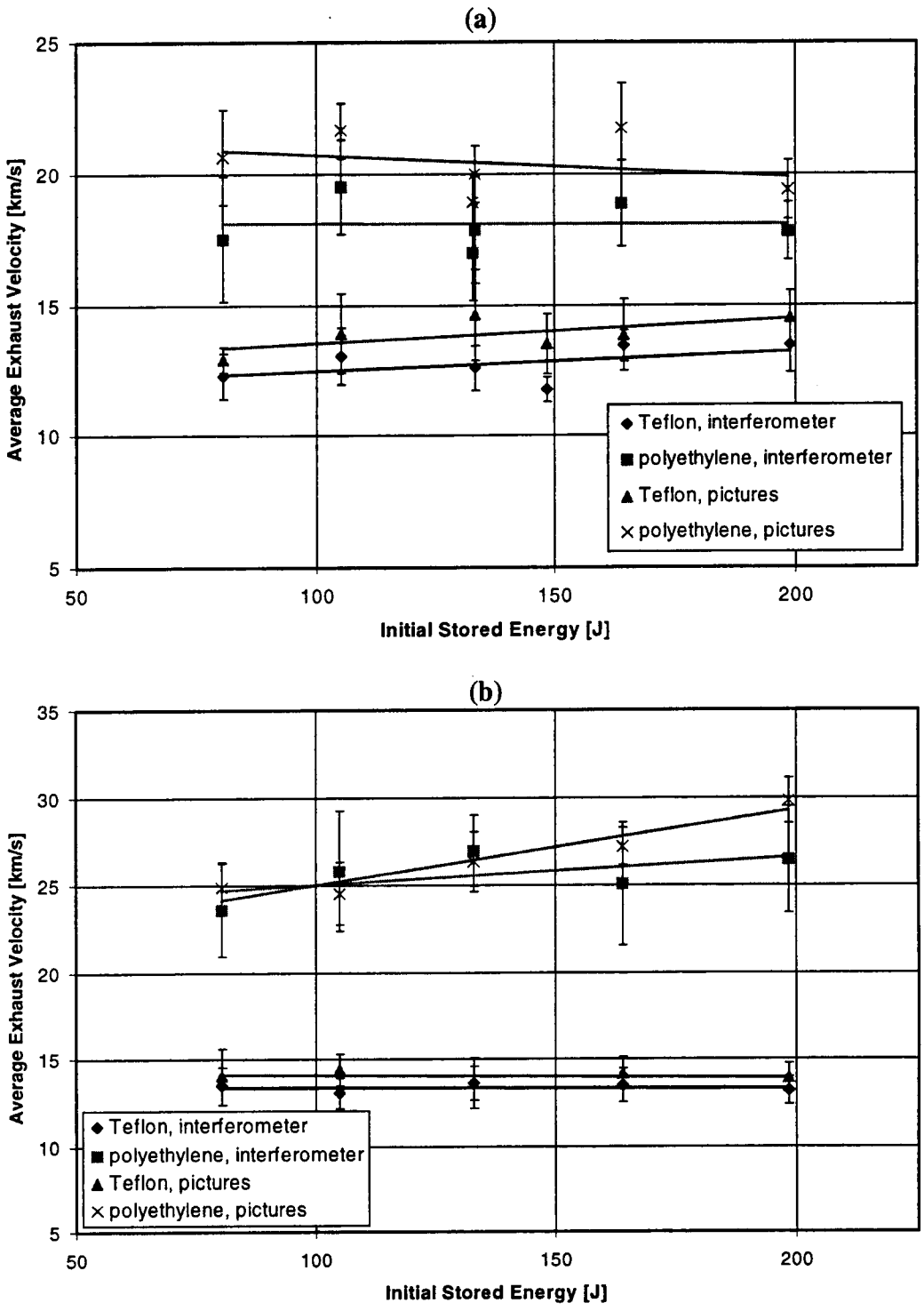

Figure 4.2.1. Average exhaust velocity as a function of initial stored energy for (a) small nozzle, (b) large nozzle.

Table 4.2.1. Summary of the average exhaust velocities for the ½ inch (small) nozzle and the ¾ inch (large) nozzle.

interferometer				picture			
Teflon		Polyethylene		Teflon		Polyethylene	
E_0 [J]	v_{ex} [km/s]	E_0 [J]	v_{ex} [km/s]	E_0 [J]	v_{ex} [km/s]	E_0 [J]	v_{ex} [km/s]
½ inch Nozzle							
80.6 (7 kV)	12.3±4.5	80.6 (7 kV)	17.5±2.4	80.6 (7 kV)	12.9±0.5	80.6 (7 kV)	20.6±1.8
105.3 (8 kV)	13.1±3.5	105.3 (8 kV)	19.5±1.8	105.3 (8 kV)	13.9±1.5	105.3 (8 kV)	21.7±1.1
133.2 (9 kV)	12.6±2.2	133.2 (9 kV)	17.9±2.0	133.2 (9 kV)	14.6±1.7	133.2 (9 kV)	20.0±1.1
148.5 (9.5 kV)	11.8±2.2	132.8 (9 kV)	17.0±1.8	148.5 (9.5 kV)	13.5±1.1	132.8 (9 kV)	18.9±1.1
164.5 (10 kV)	13.4±2.5	164.0 (10 kV)	18.9±1.6	164.5 (10 kV)	13.8±1.4	164.0 (10 kV)	21.7±1.7
199.0 (11 kV)	13.4±3.1	198.4 (11 kV)	17.8±1.1	199.0 (11 kV)	14.5±1.0	198.4 (11 kV)	19.4±1.1
¾ inch Nozzle							
80.4 (7 kV)	13.5±1.1	80.4 (7 kV)	23.6±2.7	80.4 (7 kV)	14.0±1.6	80.4 (7 kV)	24.9±1.5
105.0 (8 kV)	13.0±0.9	105.0 (8 kV)	25.8±3.4	105.0 (8 kV)	14.4±0.9	105.0 (8 kV)	24.5±1.8
132.8 (9 kV)	13.6±1.0	132.8 (9 kV)	27.0±2.0	132.8 (9 kV)	13.6±1.5	132.8 (9 kV)	26.3±1.7
164.0 (10 kV)	13.5±1.0	164.0 (10 kV)	25.1±3.5	164.0 (10 kV)	14.2±0.9	164.0 (10 kV)	27.2±1.1
198.4 (11 kV)	13.2±0.8	198.4 (11 kV)	26.4±3.0	198.4 (11 kV)	13.9±0.9	198.4 (11 kV)	29.8±1.3

The ratio of the exhaust velocities for the two different propellants is thus given by

$$\frac{v_{exp}}{v_{exT}} = \sqrt{\frac{M_{meanT}}{M_{meanp}}} = 1.89$$

with v_{exp}: exhaust velocity polyethylene

v_{exT}: exhaust velocity Teflon

M_{meanp} = 14 g/mol mean molecular weight of polyethylene

M_{meanT} = 50 g/mol mean molecular weight of Teflon.

This theoretical velocity ratio can now be compared to the experimental ratios for the different configurations. Table 4.2.2 and Figure 4.2.2 show the results of this comparison. We can see a good correlation within the error bounds. The experimental data for the large nozzle is closer to the theoretical calculated value for the ratio of the exhaust velocities. This again shows that the nozzle size is significant for the performance of the thruster when the plasma is better expanded. This result also supports hypothesis that thermal acceleration is the main contributor to the acceleration of the plasma in this thruster.

The average values for the velocity ratios are:

Large nozzle, interferometer: $v_{exp}/v_{exT} = 1.91 \pm 0.6$

Small nozzle, interferometer: $v_{exp}/v_{exT} = 1.42 \pm 0.4$

Large nozzle, pictures: $v_{exp}/v_{exT} = 1.90 \pm 0.4$

Small nozzle, pictures $v_{exp}/v_{exT} = 1.49 \pm 0.4$.

Table 4.2.2. Exhaust velocity ratios for polyethylene compared to Teflon.

interferometer				picture			
Large Nozzle		Small Nozzle		Large Nozzle		Small Nozzle	
E_0 [J]	v_{exp}/v_{exT}	E_0 [J]	v_{exp}/v_{exT}	E_0 [J]	v_{exp}/v_{exT}	E_0 [J]	v_{exp}/v_{exT}
80.4 (7 kV)	1.75±0.2	80.6 (7 kV)	1.43±0.2	80.4 (7 kV)	1.77±0.2	80.6 (7 kV)	1.60±0.2
105.0 (8 kV)	1.98±0.3	105.3 (8 kV)	1.50±0.2	105.0 (8 kV)	1.71±0.2	105.3 (8 kV)	1.56±0.2
132.8 (9 kV)	1.98±0.2	133.2 (9 kV)	1.42±0.2	132.8 (9 kV)	1.94±0.2	133.2 (9 kV)	1.37±0.2
164.0 (10 kV)	1.86±0.3	164.0 (10 kV)	1.41±0.2	164.0 (10 kV)	1.92±0.1	164.0 (10 kV)	1.57±0.1
198.4 (11 kV)	2.01±0.3	198.4 (11 kV)	1.33±0.1	198.4 (11 kV)	2.14±0.2	198.4 (11 kV)	1.33±0.2

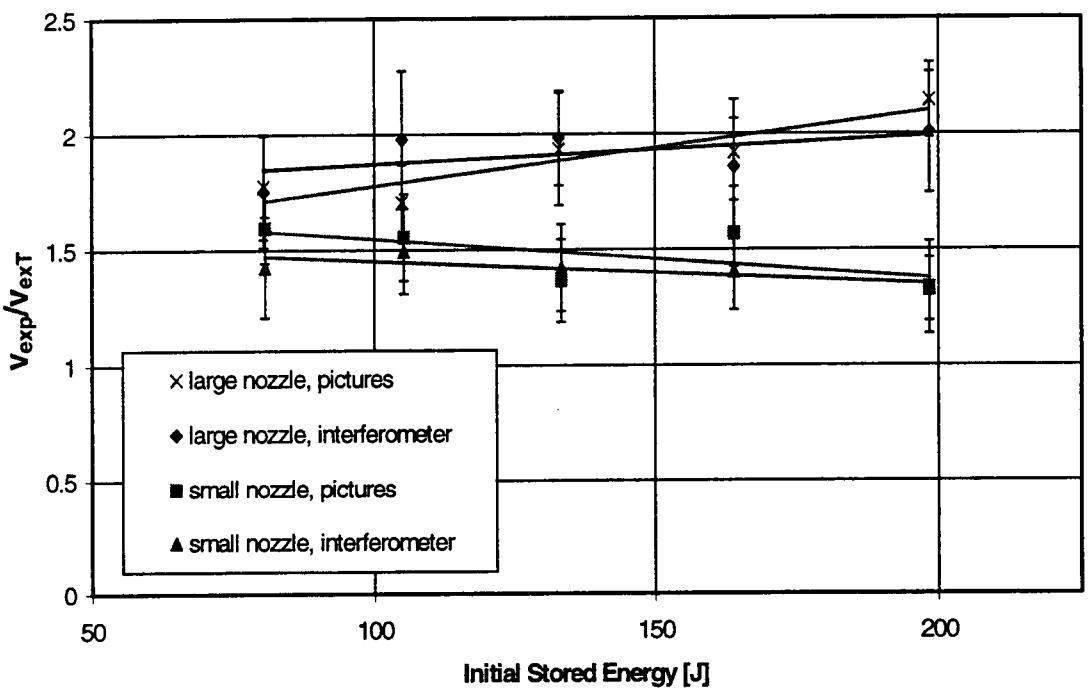

Figure 4.2.2. Ratios of the exhaust velocities of polyethylene compared to Teflon as a function of initial stored energy.

4.3 IMPULSE BIT AND SPECIFIC IMPULSE

Impulse Bit (I_{bit}) and the specific Impulse (I_{sp}), which were derived in Chapter 2, are important thruster performance parameters. The impulse bit (I_{bit}) is the total impulse for one shot and is given by

$$I_b = mv_{ex} = mI_{sp}g$$

and the specific impulse (I_{sp}) is defined as

$$I_{sp} = v_{ex}/g$$

with

v_{ex}: exhaust velocity

m: ablated mass for a single shot

g: gravitational acceleration.

Figure 4.3.1 shows the impulse bit for the two nozzle sizes as a function of the initial stored energy.

First of all, it is important to say that all the values one can see from the charts are upper limit values. The reason for this is that normally not all the ablated mass is accelerated to the same high velocities and that we likely detected the fastest velocities with our measurements. If there are slower particles, the average impulse bit and specific impulse may be significantly smaller.

The impulse bit essentially increases linearly with initial stored energy. One can see that for the small nozzle there is actually an improvement of the impulse bit for Teflon at the higher energy levels. This means that we have better performance with Teflon than with polyethylene, since we get higher impulse bit with lower energy

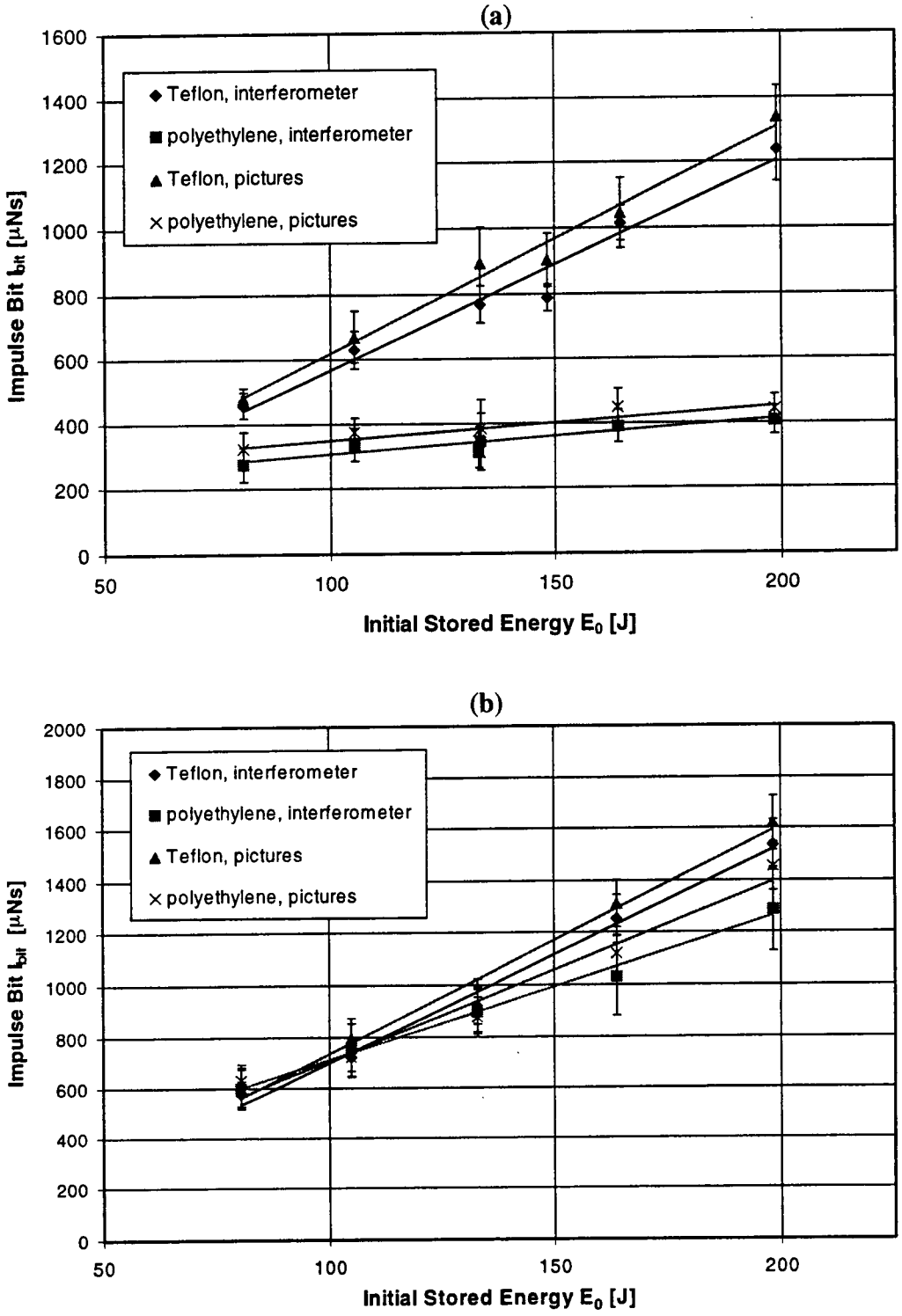

Figure 4.3.1. Impulse bit as a function of initial stored energy: (a) small nozzle, (b) large nozzle.

or we need less energy to get the same impulse bit. With this kind of nozzle configuration one can see that the advantage of the lower fuel consumption with polyethylene and the need for less stored propellant might be offset by the higher energy requirement. If a larger power supply would be required this would also require a higher weight.

At the large nozzle we could not detect a significant difference between polyethylene and Teflon for the impulse bit. The impulse bit increases with increasing initial stored energy. This can most likely be explained as more complete thermal expansion due to the large nozzle size. In this case, polyethylene would be the better propellant as less propellant is consumed, and so the propellant stored on board would be less. The power supply weight would be approximately the same for both propellants to get the same impulse bit. One can see again that the nozzle size plays a significant role in this kind of thruster.

Figure 4.3.2 shows the specific impulse as a function of initial stored energy. As expected from the velocities, the specific impulse for polyethylene is much higher than the specific impulse of Teflon. Except for the large nozzle with polyethylene as propellant the specific impulse is nearly constant over the whole energy range. One can also see a significant increase in specific impulse for the large nozzle compared to the small nozzle. This shows again that the nozzle size is an important factor for the performance of the thruster. A way to optimize the thruster is to optimize the nozzle size and maybe also the shape, here mainly the cone angle of the nozzle walls.

(a)

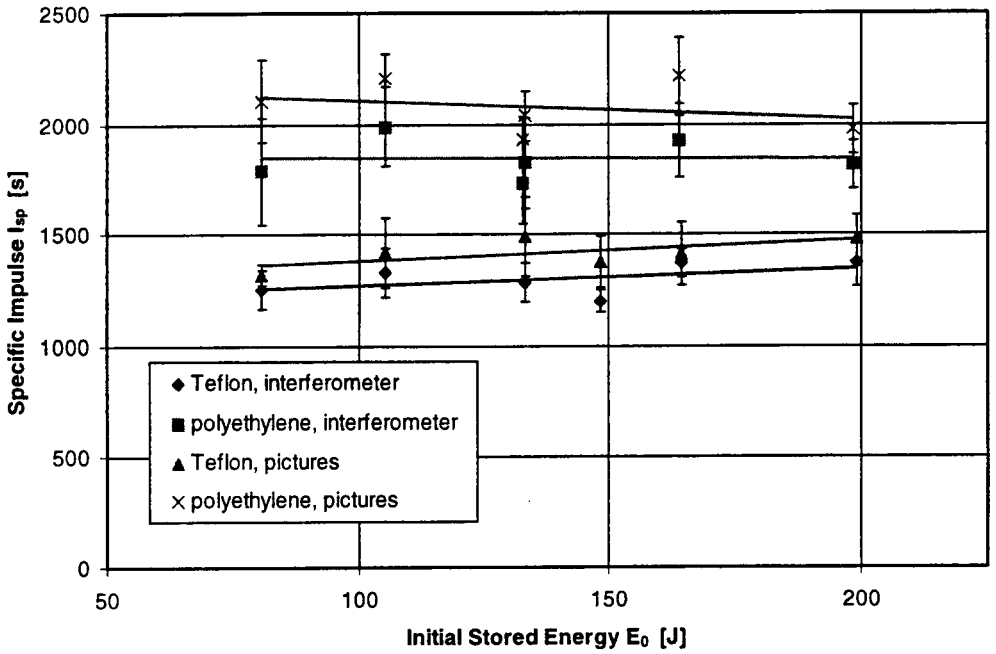

(b)

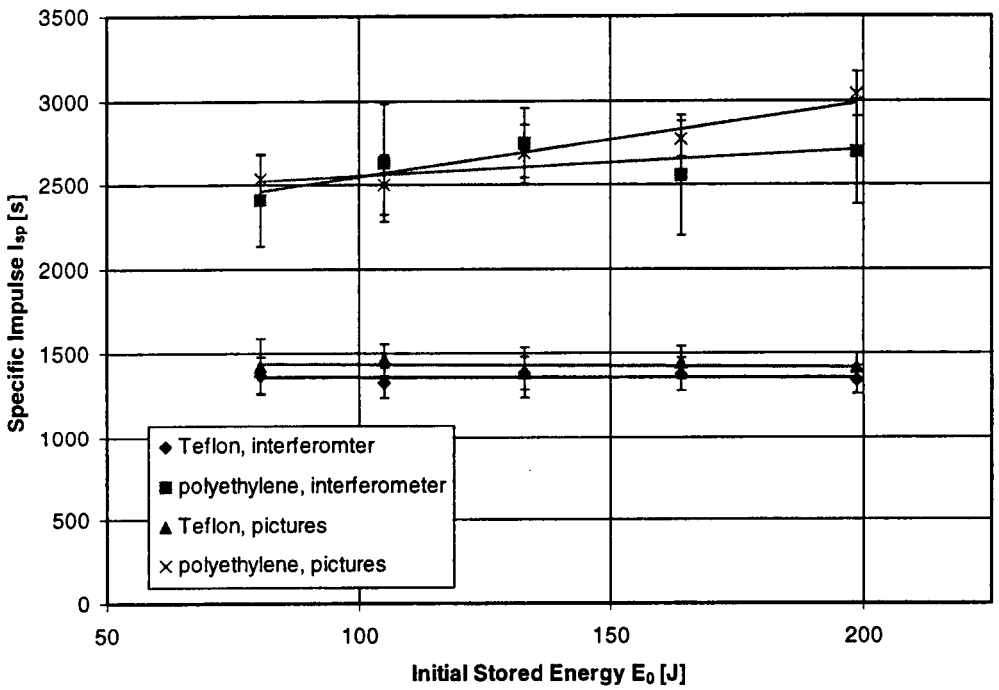

Figure 4.3.2. Specific impulse as a function of initial stored energy: (a) small nozzle, (b) large nozzle.

4.4 THRUST POWER AND EFFICIENCY

Another interesting performance parameter is the thrust power or thrust kinetic energy for a single pulse E_T. The thrust kinetic energy calculated from the mass ablation and the velocity show how much of the initial stored energy is transformed into useful exhaust kinetic energy. The thrust kinetic energy is given by

$$E_T = \frac{1}{2} m v_{ex}^2 = \frac{1}{2} m \left(I_{sp} g \right)^2 = \frac{1}{2} I_b \left(I_{sp} g \right)$$

with

m: mass ablated for a single shot

v_{ex}. Exhaust velocity

I_{sp}: specific impulse

I_{bit}: impulse bit

g: gravitational acceleration

Figure 4.4.1 shows the thrust kinetic energy for a single pulse while varying the initial stored energy.

One can see in all cases that the thrust kinetic energy increases linearly with the initial stored energy. With the small nozzle the thrust kinetic energy for Teflon is higher than the thrust kinetic energy for polyethylene.

With the large nozzle the situation changes and the thrust kinetic energy is higher with polyethylene than with Teflon as a propellant. The overall thrust kinetic energy of the large nozzle compared to the small nozzle is approximately twice as

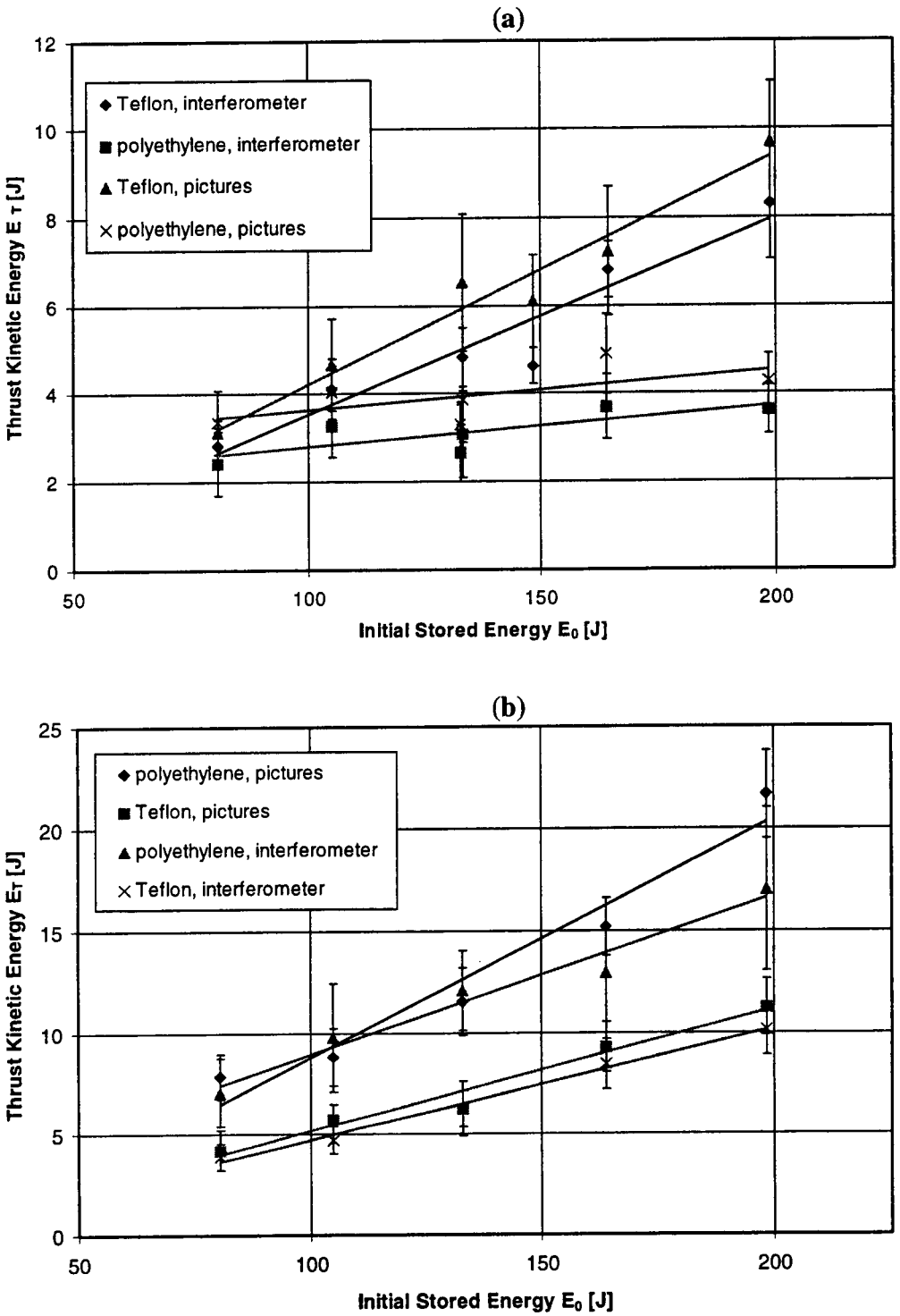

Figure 4.4.1. Thrust kinetic energy for a single pulse as a function of initial stored energy: (a) small nozzle, (b) large nozzle.

high and shows that nozzle size and shape is an important factor for the performance of the thruster.

Figure 4.4.2 shows the results from the thrust efficiency calculations. The thrust efficiency with the small nozzle is not much higher than the thrust efficiencies obtained with PPT's that have been used before. This changes with nozzle size. Since the gas is better thermally expanded in the bigger nozzle, we obtain thrust efficiencies up to 10% with polyethylene as a propellant. Polyethylene again is the better propellant choice for this type of thruster and leads us to the conclusion that the main part of the acceleration is provided by the electro-thermal acceleration rather than by electromagnetic acceleration. Since the thrust kinetic energy increased linearly with increasing initial stored energy in the measured energy range, the efficiency does not change significantly with increasing initial stored energy. Attempts to improve the overall efficiency of this type of thruster should concentrate on improving the electric circuit as will be shown in Chapter 4.6.

4.5 INTERFEROMETER ANALYSIS

Several steps were necessary to analyze the raw interferometer data in order to obtain information about the velocity, voltage and current. The current was measured with a Rogowsky coil from which we obtained the current change in time (dI/dt). With the integration of dI/dt we obtained the current curve. The voltage was directly measured.

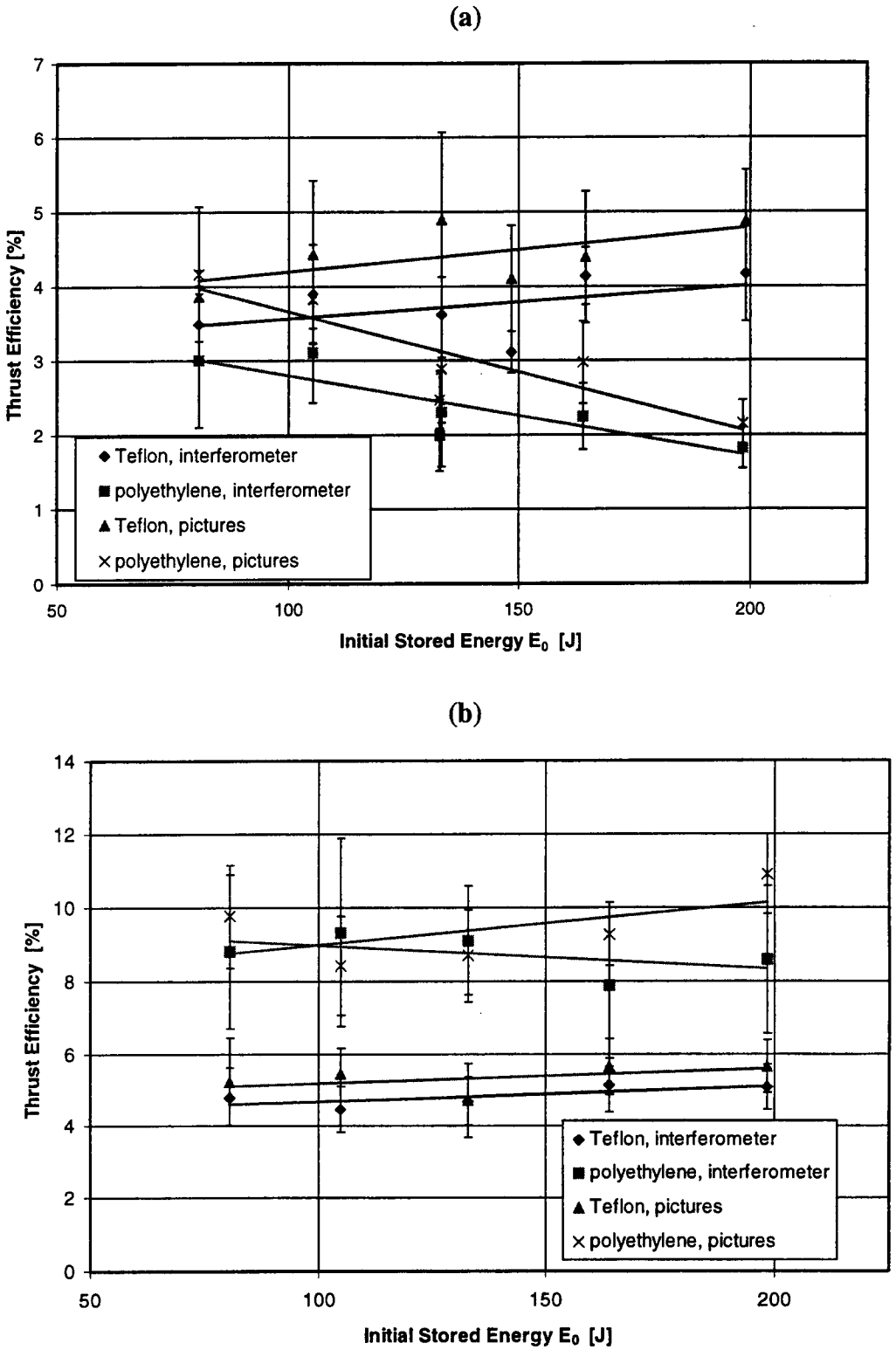

Figure 4.4.2. Thrust efficiency as a function of initial stored energy: (a) small nozzle, (b) large nozzle.

Figure 4.5.1 shows the phase shift and voltage data coming directly from the oscilloscope and the integrated current data. The first step was to set the time of the breakdown as the zero time. This point is marked with a 1 in Figure 4.5.1. The data before the breakdown was without relevance for the data we were interested in, so the data set was truncated at this point.

After the first tests, the range in which the velocities could be expected was defined and with it the time range at which the exhaust plume would cross the laser beams so that the noisy part of the recorded interferometer data could be truncated. This was necessary to work with the phase shift demodulation program and the correlation program described earlier and made the measurement more accurate. The truncation points can be seen in Figure 4.5.1 and are marked with 2 and 3. The first saturated noise spike (in front of point 2) was electric noise coming from the triggered spark gap switch and the second noise spike (after point 3) came from the crowbar switch which closed at this point.

The drop in voltage after breakdown can be explained with the position of the voltage measurement device. The voltage was measured directly across the thruster. Only voltage could be measured after current started flowing. Between the initial voltage across the capacitor and the measured voltage several devices like the triggered spark gap switch and the cables caused voltage drops, which explain the lower voltage across the thruster.

The crowbar switch should have prevented the capacitor voltage from becoming negative. The negative voltage might be explained because the crowbar

switch was not coupled closely enough to the capacitor due to the available space for the experiment. The negative voltage meant a current reversal into the capacitor and a negative charging of the capacitor. The crowbar and the series diode started working properly after the second positive voltage peak. This behavior influenced the energy that was actually dissipated into the plasma and is discussed later in this chapter.

A case for Teflon and a case for polyethylene at the same energy level of 198 J and with the same large nozzle were chosen to represent all the analyzed data and show the differences and similarities of the Teflon and polyethylene data. The Pictures 4.5.1 and 4.5.2 show the expansion of the exhaust plume with time of the cases mentioned above. The time between the frames was 1 μs. From the distance

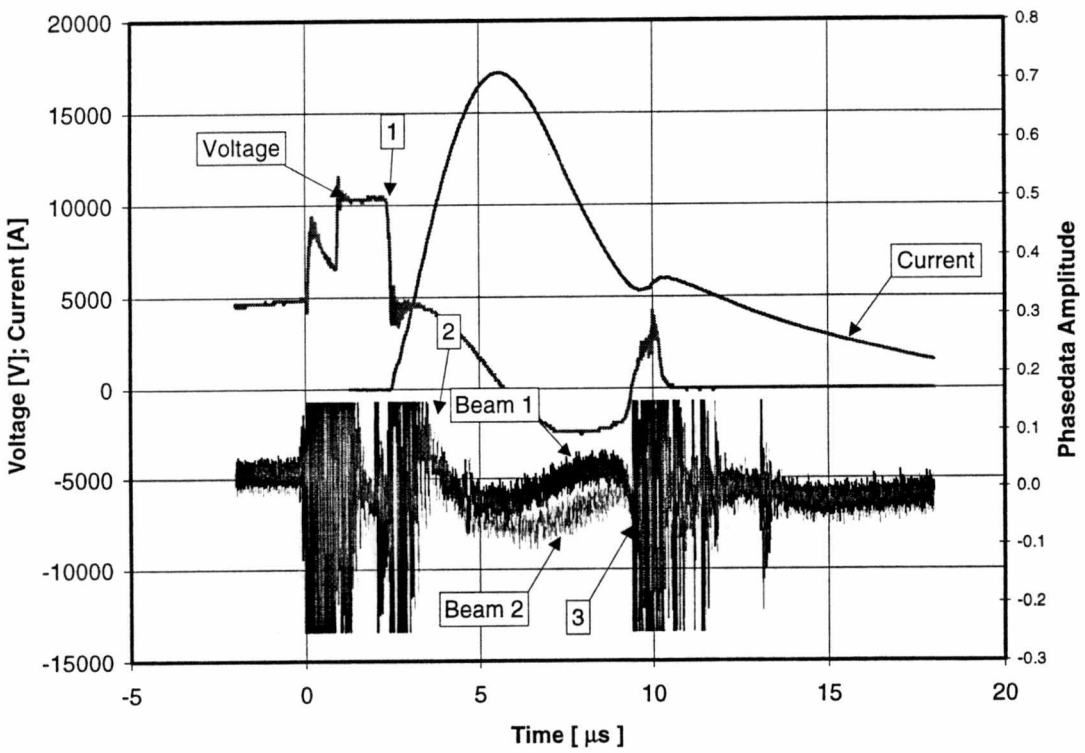

Figure 4.5.1. Oscilloscope data with significant truncation points.

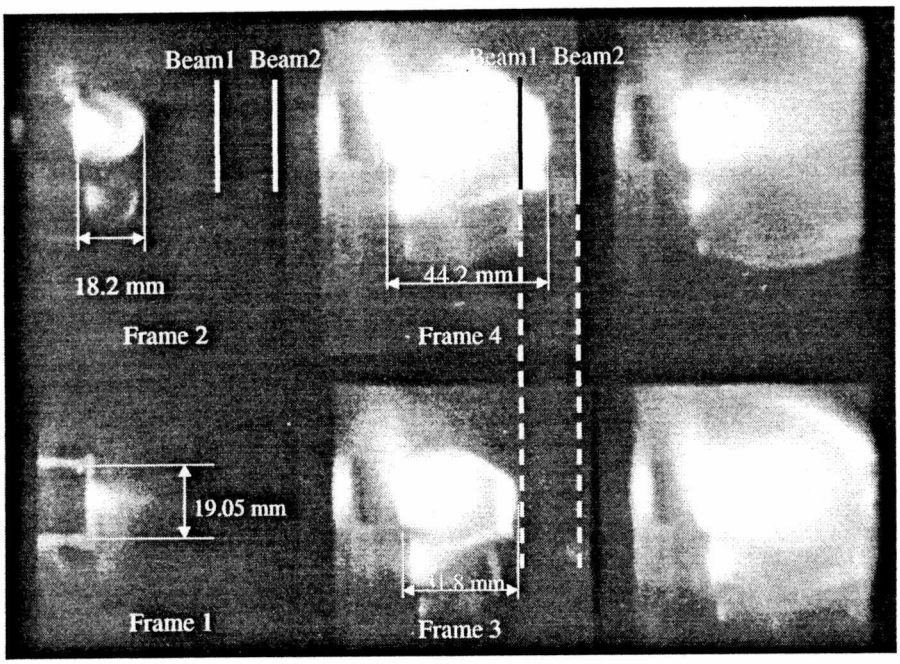

Plate 4.5.1. Picture of the exhaust plume of a Teflon shot at an initial stored energy level of 198 J for the large nozzle with an interframe time of 1 μs.

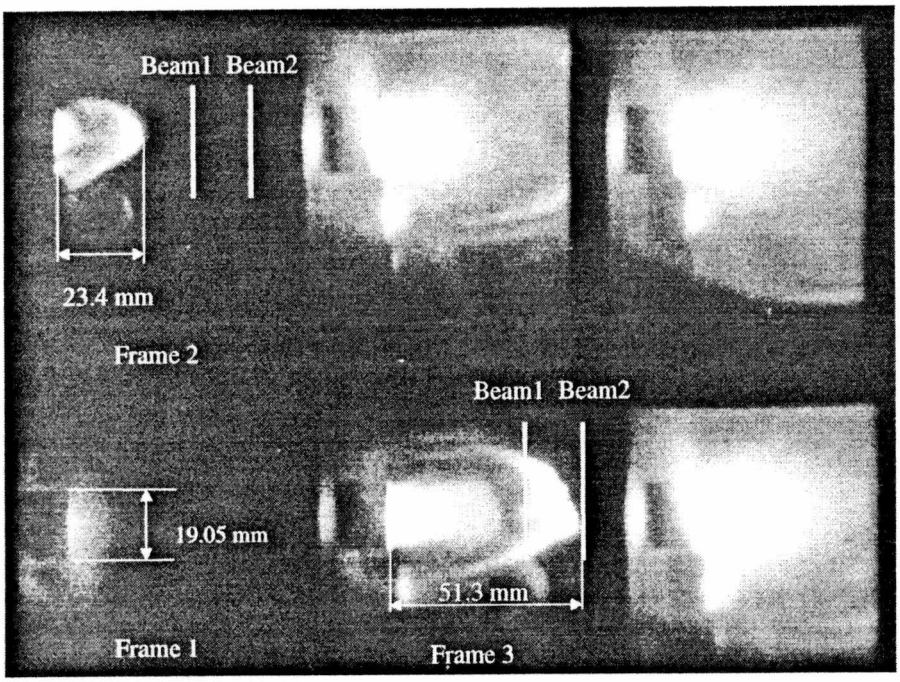

Plate 4.5.2. Picture of the exhaust plume of a polyethylene shot at an initial stored energy level of 198 J for the large nozzle with an interframe time of 1 μs.

traveled and the time difference of the frames we were able to calculate the velocity. The pictures were scanned into a computer and expanded to provide a more accurate measurement of the distances. In order to calculate the distance traveled by the plasma the outer diameter of the nozzle was taken as a reference length. With the outer diameter as a known length and the number of pixels from the scanned pictures we were able to calculate the distance traveled of the exhaust plume. The measurements of the distance were made from the exit of the nozzle to the front of the visible shockwave of the exhaust plume. Only the first three to four frames were useful, since after this time the shock front extended beyond the field of view of the camera.

Figures 4.5.2 and 4.5.4 show the truncated current and voltage data with the phase shift peaks of the interferometer beams. The time was set to zero at the point the breakdown occurred and allows us a direct comparison of the different data with respect to time. Using the time separation of the phase shift peaks of the interferometer beams and the distance of 14mm between the beams we were able to calculate the velocity of the exhaust plume. Therefore, a correlation program was used as mentioned before. This program used the phase shift shape of beam 1 and moved it on the time scale to the best fit with the phase shift shape of the beam 2. The time difference for the best fit was used to calculate the exhaust velocities. Figures 4.5.3 and 4.5.5 show the correlation program output.

The exhaust velocity was also calculated directly from the time difference of the phase shift peaks as a control and was close to the correlation velocity, although

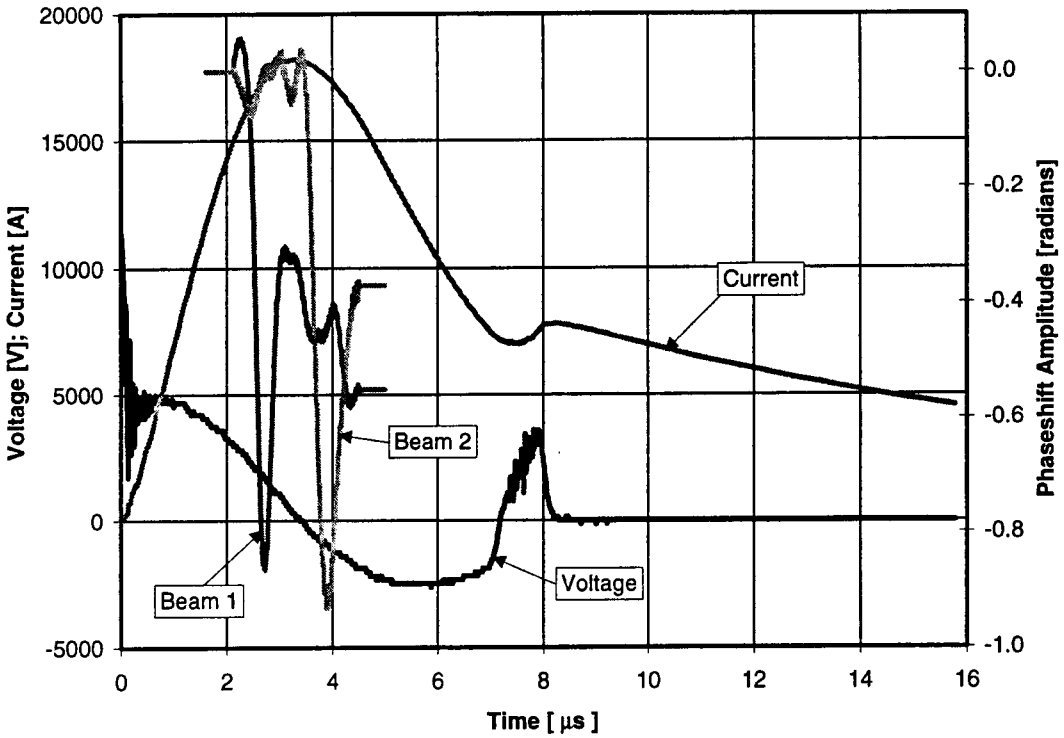

Figure 4.5.2. Current, voltage and demodulated phase shift data of a Teflon shot with an initial stored energy of 198 J for the large nozzle.

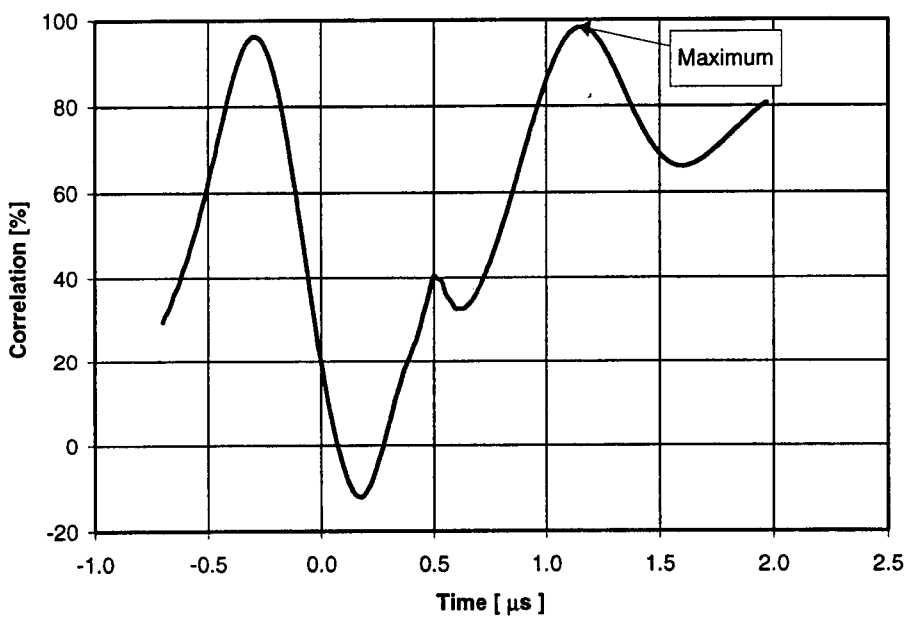

Figure 4.5.3. Correlation curve of the phase shift data of the Teflon shot in Figure 4.5.2.

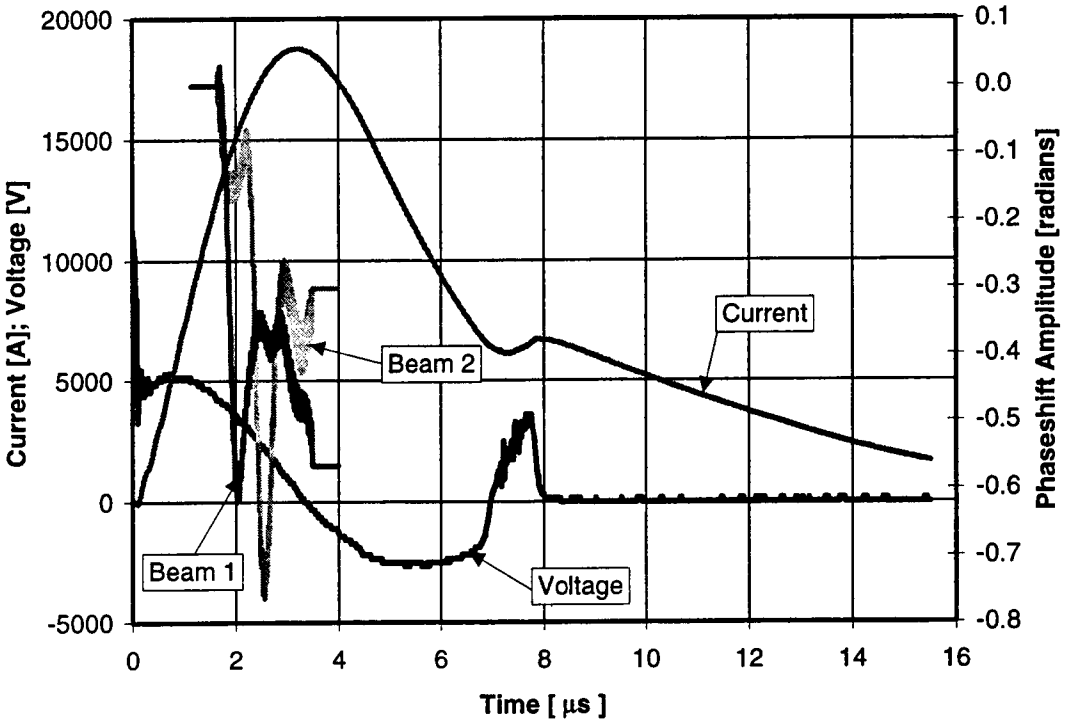

Figure 4.5.4. Current, voltage and demodulated phase shift data of a polyethylene shot with an initial stored energy of 198 J for the large nozzle.

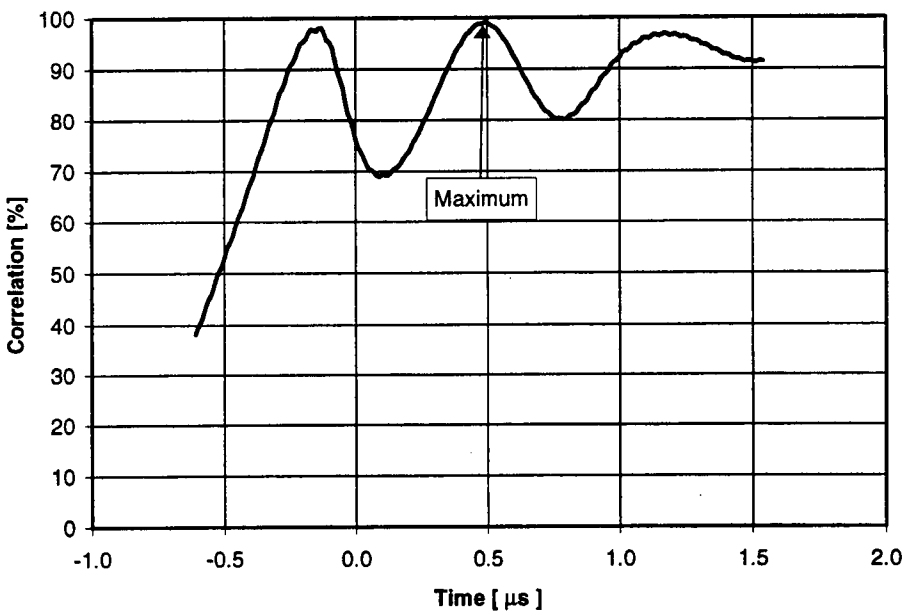

Figure 4.5.5. Correlation curve of the phase shift data of the polyethylene shot in Figure 4.5.4.

this method was not as accurate as the use of the correlation program. The correlation program showed a big advantage and a higher accuracy especially for the noisier shots where the peaks were not narrow, and a curve fit was better than only a peak fit.

Picture 4.5.1 shows the exhaust plume of a shot with Teflon at an initial stored energy of 198 J for the large nozzle. Frame 1 shows the approximate time at which the breakdown occurred and can be related to the zero time in Figure 4.5.2. Frame 2 was taken at approximately 1 μs, frame 3 at 2 μs and frame 4 at 3 μs after breakdown. In frame 4 the exhaust plume has already reached the first interferometer beam. The velocity calculated with frame 2 and frame 3 was 13.6 km/s and the velocity calculated from frame 3 and frame 4 was 12.4 km/s. The velocities match the velocities calculated with the interferometer data within the error bounds.

Figure 4.5.2 shows the interferometer data set belonging to Picture 4.5.1. We can see the phase shift peaks of the interferometer beams occurring at 2.7 μs for beam 1 and at 3.9 μs for beam 2. The velocity measurement took place close to the time of the maximum current. The velocity calculated directly from the phase shift peaks was 11.7 km/sec. Figure 4.5.3 shows the output curve of the correlation program. The peak in correlation was at 1.16 μs with a value of 99.27 %. With this correlation time we calculated a velocity of 12.1 km/sec. The two velocity values from the interferometer data and the velocity calculated from the pictures match within the error bounds.

Picture 4.5.2 shows a shot with polyethylene as propellant with an initial stored energy of 198 J for the large nozzle and relates to figure 4.5.4. One can see from the

pictures that the exhaust plume traveled farther downstream in every frame than the exhaust plume of Teflon in picture 4.5.1. Therefore, we only had two frames by which to calculate the velocity since the shockfront had already left the field of view at frame 4. Frame 1 shows again the time of breakdown and was used as zero time. The velocity was calculated with frame 2 and frame 3 and was 27.9 km/s. This matched the calculated velocity from the interferometer data within the error bounds. Frame 2 was approximately 1 μs and frame 3 approximately 2μs after breakdown. The exhaust plume reached the first interferometer beam at frame three.

One can see the difference between the exhaust plume of polyethylene and Teflon. The polyethylene plume is far more stretched out than the Teflon plume, which is an effect of the higher velocity. The Teflon plasma has a more conical shape. Differences between the velocities from the pictures and the velocities from the interferometer can sometime also be explained by the unsymmetrical shape of the exhaust plume. It might have been that the plume axis did not cross the interferometer beams, and this would have resulted in a lower velocity.

Figure 4.5.4 shows the voltage and current curves with the peaks of the demodulated phase shift data. As the polyethylene plasma was much faster than the Teflon plasma, the velocity measurement took place shortly before the maximum current. One can clearly see that the phase shift peaks of the polyethylene shot occurred earlier than the peaks of the Teflon shot, which shows the difference of the exhaust velocities. For this shot the peaks were measured at 2.04 μs for interferometer beam 1 and at 2.55 μs for beam 2. This gave us an exhaust velocity of 27.5 km/s.

Figure 4.5.5 shows the output curve of the correlation program for the same shot. The peak in correlation occurred at 0.49 μs with a value of 99.07 %. A velocity of 28.6 km/s was calculated. Here also, the velocities calculated from the picture and from the interferometer data matched within the error bounds.

4.6 POWER AND DISSIPATED ENERGY

The power curve was calculated from the recorded oscilloscope data of the current and the voltage. By integrating the power curve we obtained the energy as a function of time. As the voltage and current were measured directly across the thruster, the power and energy gave us information about the actual thruster input. Figure 4.6.1 shows the power and current curve for the Teflon case of Section 4.5 and Figure 4.6.2 shows the power and current for the polyethylene case of Section 4.5.

The negative part of the power curve represents the voltage reversal in the power circuit and the negative charging of the capacitor. The second positive peak shows that the capacitor was charged positive again and added some more energy to the plasma. This can especially be seen from the energy curve.

The actual dissipated energy into the plasma was the value obtained after the power dropped to zero and can be seen as a zero offset of the energy curve. Without the second positive power peak the dissipated energy would have been even smaller and occurred as a minimum of the energy curve at the time of the second zero crossing

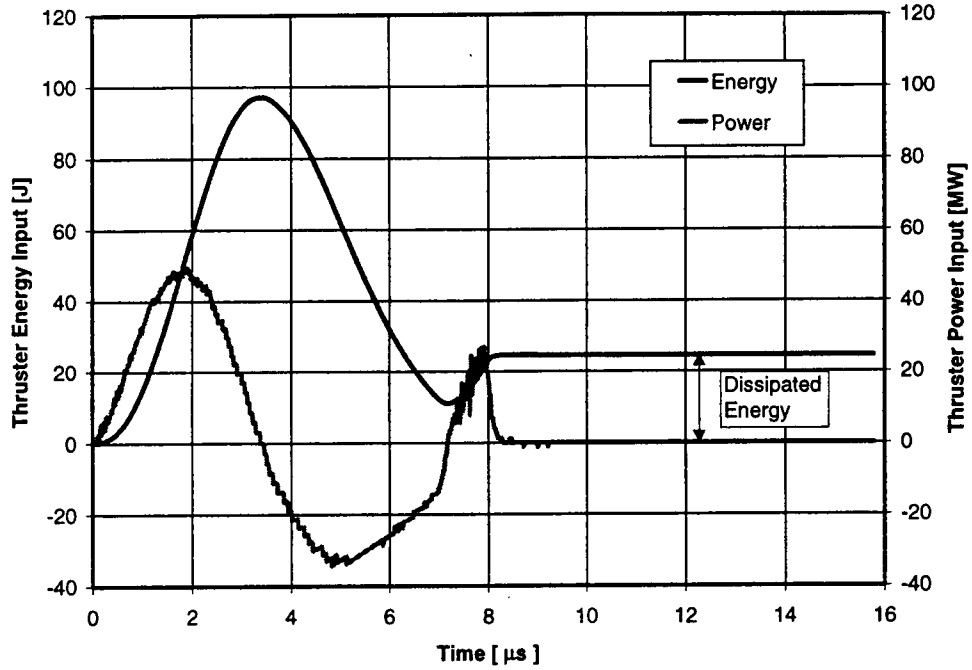

Figure 4.6.1. Power and energy thruster input as a function of time for a Teflon shot with an initial stored energy of 198 J for the large nozzle.

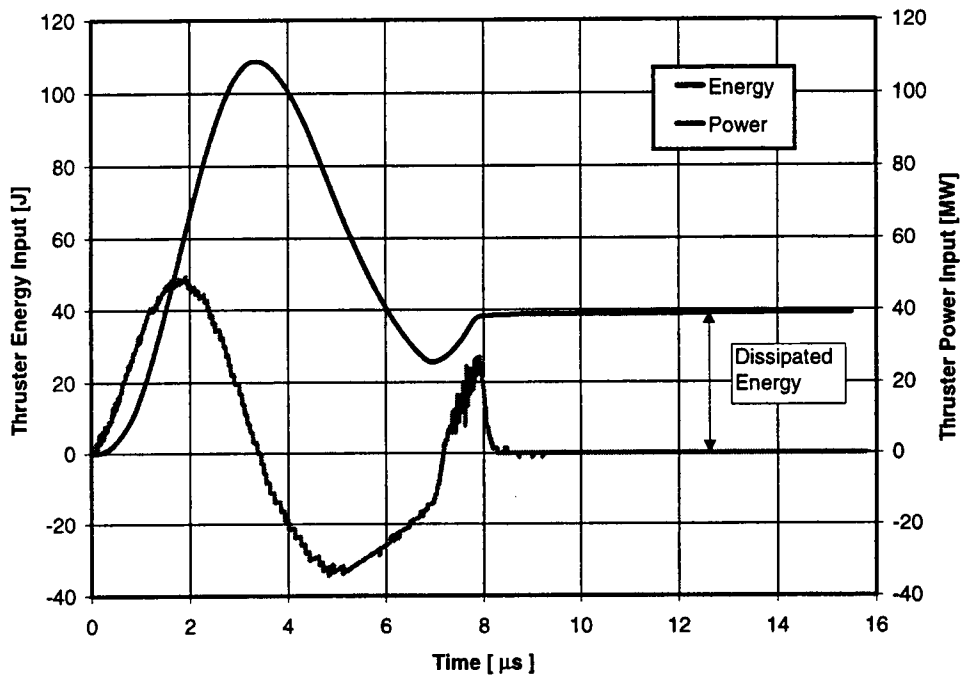

Figure 4.6.2. Power and energy thruster input as a function of time for a polyethylene shot with an initial stored energy of 198 J for the large nozzle.

of the power curve. The added energy from the second positive power peak was the value from the energy minimum to the constant line at the end of the energy curve.

Approximately half of the initial stored energy was lost in the external power circuit to the thruster, since the main energy peak was only approximately half the value of the initial stored energy. This can be explained with changing magnetic fields. While dI/dt from the equations given below is positive (positive slope) magnetic field energy is stored in the thruster. This energy is not dissipated into the plasma. When dI/dt becomes negative (negative slope) the stored magnetic field energy in the thruster goes out again and allows the magnetic field to collapse. Most of the energy was lost in this process and only a fraction of the initial stored energy could be dissipated into the plasma and used for the acceleration of the plasma. This can be seen from the equations for the voltage and power. The voltage is given by

$$V = IR + L\frac{dI}{dt} + I\frac{dL}{dt},$$

and the power is given by

$$P = IV = I^2R + LI\frac{dI}{dt} + I^2\frac{dL}{dt}.$$

Only the first term of each equation was useful for thermal heating, as the second and the third terms of the equations cancelled each other out over the time, due to the positive and negative swings of the voltage and the positive and negative slopes of the current.

The first term integrated represented the dissipated energy into the plasma and can be written as

$$E_{diss} = \int_0^t P = \int_0^t IV = \int_0^t I^2 R .$$

One can see a difference between Teflon and polyethylene. With polyethylene the actual dissipated energy and the energy in the second half of the power circuit was higher than for Teflon. This probably meant that the internal resistance of the polyethylene plasma was higher than the internal resistance of the Teflon plasma. This can also be explained with the equations shown before. Only the first term is relevant for the acceleration and heating of the plasma. As the current was nearly the same for Teflon and for polyethylene, the only difference could be in the plasma resistance of the propellants.

A term for the thermal efficiency of the thruster was determined and can be written as

$$\eta_{Th} = \frac{E_T}{E_{diss}} .$$

An example can be given with the two cases mentioned above. For the Teflon case we got a dissipated energy of 25 J. With an thrust kinetic energy at this power level of approximately 11 J a thermal efficiency of 44 % can be calculated.

For the polyethylene case mentioned earlier we got a dissipated energy of approximately 40 J. A thrust kinetic energy of approximately 20 J was measured at this energy level what results in an thermal efficiency of approximately 50 %.

One can see that we got a slightly higher thermal efficiency with polyethylene as propellant than with Teflon, but this is only an example and more shots should be examined to give a more correct estimate of the thermal efficiency. This example shows very well that in to improve the overall efficiency of the thruster one should concentrate in improving the electric circuit, as a thermal efficiency of up to 50 % is already very good but the overall efficiency is still not higher than 10 %.

The velocities with polyethylene were approximately twice as high as the exhaust velocities of the Teflon plasma. As the dissipated energy into the polyethylene plasma was not twice as high as the dissipated energy into the Teflon plasma the higher exhaust velocities of the polyethylene plasma were a result of the combination of higher energy input and lower mean molecular weight.

4.7 ELECTRON NUMBER DENSITY

We were also able to calculate an estimate for the electron number density from the phase shift data. A relation between the electron number density and the phase shift was derived as shown in Chapter 2. For the He-Ne laser with a wavelength of 633 nm the electron number density is given by,

$$N_e = 5.59e20 * \frac{\Delta\varphi}{d}\left[m^{-3}\right]$$

with

N_e: electron number density

$\Delta\varphi$: phase shift (radians)

d: effective path length.

The effective path length was measured from the pictures. The two cases already discussed above were also taken to calculate some examples for the electron number densities.

The effective path length for the first interferometer beam in the Teflon case at 198 J was approximately 27 mm. With a peak phase shift of 0.865 [radians] this results in an electron density of approximately 1.8e22 [m^{-3}].

The effective path length for the first interferometer beam in the polyethylene case at 198 J was approximately 26 mm. With a peak phase shift of 0.62 [radians] an electron number density of approximately 1.3e22 [m^{-3}] was obtained. Further investigation and analysis of all the data would give a better insight into the behavior of the electron density with changing initial stored energy and different propellants.

Figure 4.7.1 shows the change of electron number density with time. The shapes are similar to the phase shift shapes, since a constant effective path length was assumed, so that only the phase shift changed with time. One can see that the peak electron number density of Teflon is significantly higher than the electron number density of polyethylene. The shapes of the electron number density data look similar to the shapes of the current data.

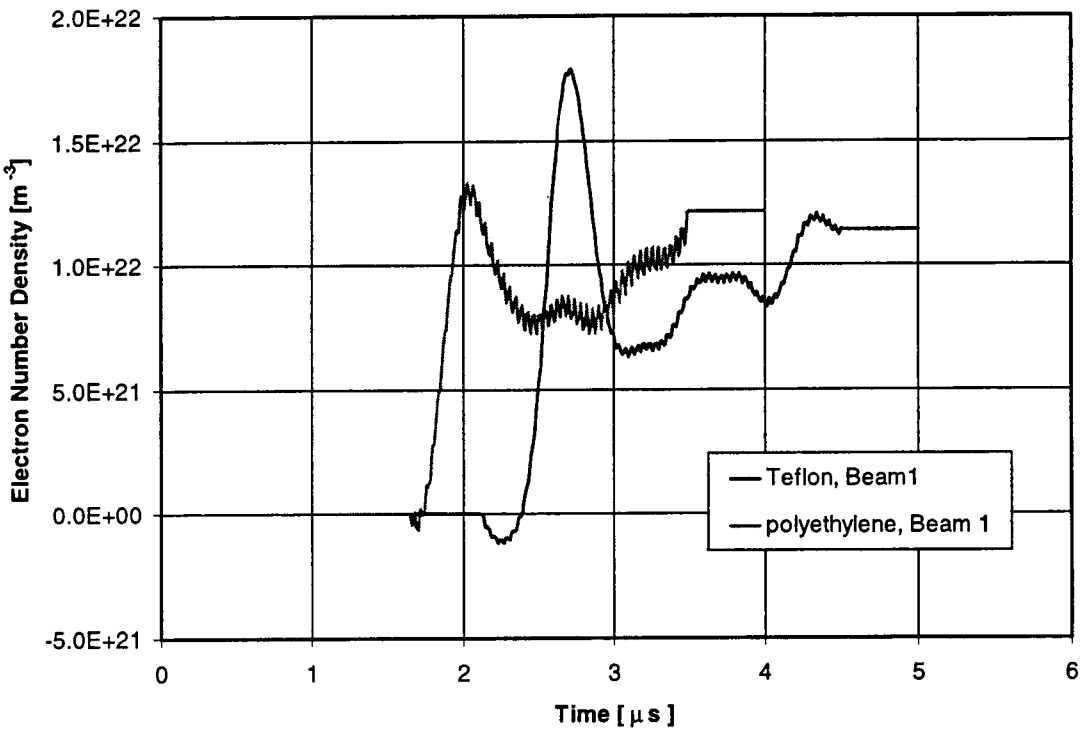

Figure 4.7.1. Electron number density as a function of time for each first beam of a Teflon and a polyethylene shot with an initial stored energy of 198 J for the large nozzle.

4.8 SPECTROSCOPIC DATA

Figure 4.8.1 shows typical spectrometer data for Teflon and polyethylene with an initial stored energy of 132.8 J for the large nozzle with species lines labeled. The data only show a restricted area of the wavelength. We only made a tentative identification of the lines and the species involved.

A more detailed analysis of the spectrum of the plasma would be of interest, especially the appearance of the different species in time. A wider bandwidth would have been better able to detect all the species present in the plasma. This was beyond the scope of this thesis.

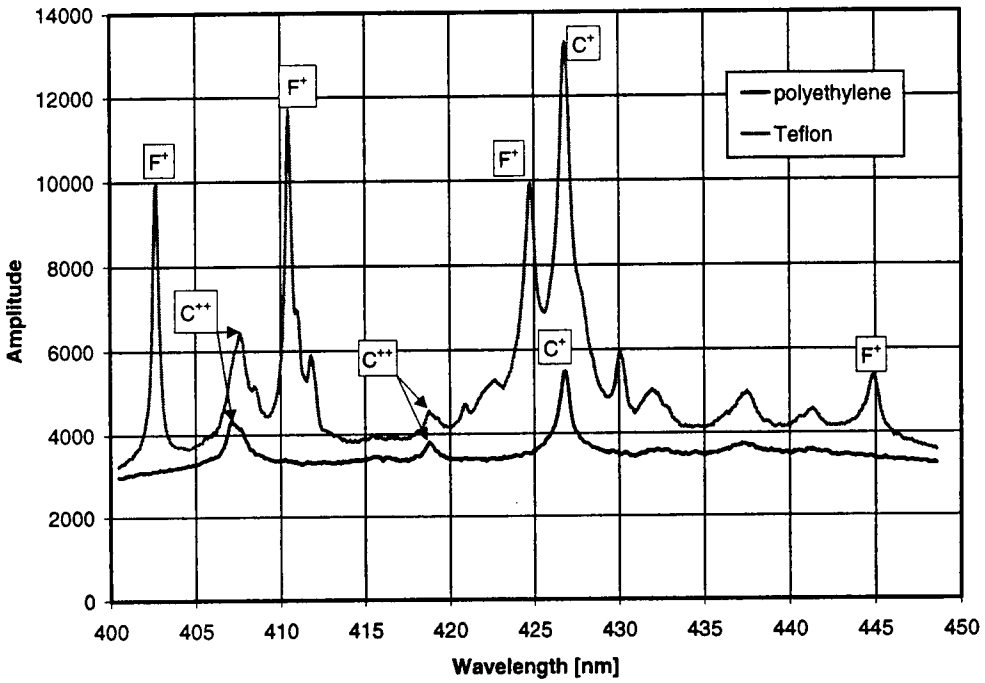

Figure 4.8.1. Spectroscopic data for a Teflon and a polyethylene shot with an initial stored energy level of 132.8 J for the large nozzle.

CHAPTER 5

SUMMARY/ CONCLUSIONS

The experiments fulfilled our expectations and supported the hypothesis that in a coaxial pulsed plasma thruster the electrothermal processes are the main contributors for the acceleration of the propellant plasma. Several experimental configurations provided a basis for the analysis of the thruster. Two different nozzle sizes were used, one with a nozzle exit diameter of 0.5 in (1.27 cm) and one with a nozzle exit diameter of 0.75 in (1.91 cm). For both sizes Teflon and polyethylene were tested as propellants to show the difference in performance in terms of mean molecular weight. Also a range of energy levels was covered to observe the influence of the initial stored energy on the thruster behavior. Data such as velocity, mass ablation, current and voltage were measured and several important thruster parameters were calculated with these measurements. The velocity was measured with a two beam laser interferometer and with pictures using a high speed camera. The results showed that the thruster performed better with polyethylene as a propellant by approximately a factor of two than with Teflon in terms of exhaust velocity, specific impulse and thrust efficiency.

The mass ablation occurred as expected and was linear with the initial stored energy. Less polyethylene was ablated than Teflon, which may have been result of a soot layer consisting of carbon particles over the nozzle walls that may have been

present in the experiments with polyethylene. The influence of the soot layer could also be seen from the behavior of the energy flux, which was larger for Teflon than for polyethylene.

Much higher exhaust velocities could be achieved with polyethylene as propellant than with Teflon. The velocity was also influenced by the nozzle size so that higher velocities were measured using the larger nozzle. The velocity changes with changing initial stored energy were not very large. In the case of the small nozzle velocities in the range of 18 to 21 km/s with polyethylene and 12 to 14 km/s were measured. The use of the large nozzle resulted in exhaust velocities of 24 to 29 km/s in the case of polyethylene and of 13 to 14 km/s for Teflon. The results for the velocity obtained from the pictures and from the interferometer matched within the error bounds of the measurement. It could be shown for the large nozzle that the ratio of the exhaust velocities of polyethylene to Teflon matched with the derived relation of the mean molecular weights of the propellants within the error bounds.

We found that the impulse bit for Teflon was higher than the impulse bit for polyethylene, especially in the case of the small nozzle. In the case of the large nozzle the resulting impulse bits were nearly equal for both propellants. The impulse bit was found to increase linearly with increasing initial stored energy. Impulse bits in the range of 600 to 1600 μNs were calculated for Teflon and polyethylene in the case of the large nozzle.

The specific impulse was higher for polyethylene than for Teflon due to the higher velocities that were achieved with polyethylene. This was true for both nozzle

sizes. The specific impulse was higher for both propellants in the case of the large nozzle compared to the small nozzle. The specific impulse was 1400 s for the small nozzle using Teflon and 2100 s for the small nozzle using polyethylene. The specific impulse did not change significantly in the case for Teflon using the large nozzle, but we obtained a specific impulse up to 3000 s with polyethylene as propellant using the large nozzle.

The thrust kinetic energy obtained from the mass ablation and velocity data was higher for Teflon than for polyethylene using the small nozzle. This reversed when using the large nozzle and the thrust kinetic energy calculated for polyethylene was significantly higher than the thrust kinetic energy for Teflon.

The same behavior was found for the thrust efficiency, which was defined as the ratio of thrust kinetic energy to initial stored energy. Thrust efficiencies of up to 5% for Teflon and 3% for polyethylene were obtained using the small nozzle. In the case of the large nozzle we obtained thrust efficiencies of approximately 10% with polyethylene as propellant and 5% with Teflon as propellant.

We found also that the dissipated energy into the propellant was very small compared to the initial stored energy. The dissipated energy into the polyethylene plasma was significantly higher than the dissipated energy into the Teflon plasma, which leads to the conclusion that the internal resistance of the polyethylene plasma was higher than the internal resistance of the Teflon plasma. We also measured a relatively high thermal efficiency of up to 50% that was significantly higher than the

overall efficiency of the thruster with up to 10%. Up to 60% of the thruster input energy was lost in magnetic fields in the thruster.

Sample electron number densities of the plasmas were calculated for both propellants. We obtained approximately 1.8e22 (m^{-3}) for Teflon and 1.3e22 (m^{-3}) for polyethylene.

The results showed that to improve the thruster the main effort should be made with respect to the ignition and power circuit of the thruster as approximately 50 % of the initial stored energy was lost in the external circuit before the thruster input. An increase in thermal efficiency might be achieved by optimizing the nozzle size. Further investigation of the influence in nozzle shape, mainly the cone angle of the walls should be made to see if an increase in efficiency can be achieved. One can see from the results that the right choice for the propellant is one of the main parameters in the development of a coaxial pulsed plasma thruster. Further investigation in this area should be made to optimize this kind of thruster.

To enable a reliable repeatability of the shots a better power source has to be designed. The main concern should be the allowable voltage, which should be approximately 30 kV to 40 kV to obtain reliable breakdown without the use of a trigger pulse.

The detectors of the interferometer should be better protected against electric noise in order to improve the velocity measurements, which came especially from the spark gap switch and the crowbar. This would also make it possible to measure the velocities closer to the exit of the nozzle.

In order to obtain a higher dissipated energy into the plasma, the whole power supply should be designed to be more compact in order to keep the inductance low. The high inductance of the ignition circuit was a result of the long coaxial cables that were used to connect all the circuit parts. This would also result in a closer coupling of the crowbar switch to the energy storage capacitor and would prevent the voltage from becoming negative. This would protect the energy storage capacitor from being charged negatively and would result in a longer lifetime.

LIST OF REFERENCES

LIST OF REFERENCES

[1] Stuhlinger, E.: "Ion Propulsion for Space Flight," chap.1, McGraw-Hill Book Company, New York, 1964.

[2] Oberth, H.: "Man into Space," Harper & Row, Publishers, Incorporated, new York, 1957.

[3] Stuhlinger, E.: Possibilities of Electrical Space Ship Propulsion, *Ber. 5th Intern. Astronaut. Kongr.,* Innsbruck, p.100, August, 1954.

[4] Stuhlinger, E.: Electrical Propulsion Systems for spaceships with Nuclear Power Source, *J. Astronaut.*, vol.2, p. 149, 1955; vol. 3, pp. 11, 33, 1956.

[5] Stuhlinger, E.: Flight Path of an Electrically Propelled Space Ship, *Jet Propulsion*, vol. 27, no. 4, p. 410, April, 1957.

[6] Jahn, Robert G.: "Physics of Electric Propulsion," McGraw-Hill Book Company, New York, 1968.

[7] Auweter-Kurtz, M.: "Lichtbogenantriebe fuer Weltraumaufgaben," B.G. Teubner Stuttgart, 1992.

[8] Cybulski, R. J., et al.: Result from SERT 1 Ion Rocket Flight Test, *NASA Tech. Note* D-2718, 1965.

[9] Vondra, R., Thomassen, K., Solbes, A.: "Analysis of Solid Pulsed Plasma Thruster," AIAA Paper No. 70-179, AIAA 8th Aerospace Sciences Meeting, New York, N.Y./ January 19-21, 1970.

[10] Auweter-Kurtz, M.: "Elekrtische Raumfahrtantriebe," (Manuskript zur Vorlesung als Zusatz zum dem Lehrbuch "Lichtbogenantriebe fuer Weltraumaufgaben), B.G. Teubner Verlag, Stuttgart, 1993.

[11] Messerschmid, E.: " Vorlesungsmanuskript Grundlagen der Raumfahrtsysteme," Institut fuer Raumfahrtsysteme (IRS) Universitaet Stuttgart, 1995.

[12] Keefer, D., Rhodes, R.: "Electromagnetic Acceleration in Pulsed Plasma Thrusters," IEPC 97-035, 25th International Electric Propulsion Conference, Cleveland, Ohio, August, 1997.

[13] Kamhawi, H., Turchi, P.J., Leiweke, R.J.: "Design and Operation of a Laboratory Bench-Mark PPT," AIAA 96-2732, 32nd AIAA/ASME/SAE/ASEE Joint Propulsion Conference and Exhibit, July 1-3, 1996/ Lake Buena Vista, FL.

[14] Bobrow, L. S., "Fundamentals of Electrical Engineering," p. 151 ff., Oxford University Press, Inc., 1996.

[15] Rashleigh, S. C., and Marshall, R. A., "Electromagnetic Acceleration of Macroparticles to High Velocities," J. Appl. Phys., Vol. 49, pp 2540-2542, 1978.

[16] Holt, E. H., Haskell, R. E., "Foundations of Plasma Dynamics," Chapters 9, 11.2, The Macmillan Company, New York, 1965.

[17] Pope, R. B., "Simplified Computer Model for Predicting the Ablation of Teflon," J. Spacecraft, Vol. 12, No.2, pp 83-88, Feb. 1975.

[18] Leung, C.H., Staggs, J.E.J., Brindley, J., McIntosh, A.C., "Modelling of a One Dimensional Ablation Process with Char Formation," Combust. Sci. and Tech., 1996, Vol. 119, 99.301-329, Overseas Publishers Association.

BIBLIOGRAPHY

BIBLIOGRAPHY

Auweter-Kurtz, M.: "Lichtbogenantriebe fuer Weltraumaufgaben," B.G. Teubner Stuttgart, 1992.

Auweter-Kurtz, M.: "Elekrtische Raumfahrtantriebe," (Manuskript zur Vorlesung als Zusatz zum dem Lehrbuch "Lichtbogenantriebe fuer Weltraumaufgaben), B.G. Teubner Verlag, Stuttgart, 1993.

Bobrow, L. S., "Fundamentals of Electrical Engineering," p. 151 ff., Oxford University Press, Inc., 1996.

Holt, E. H., Haskell, R. E., "Foundations of Plasma Dynamics," The Macmillan Company, New York, 1965.

Jahn, Robert G.: "Physics of Electric Propulsion," McGraw-Hill Book Company, New York, 1968.

Messerschmid, E.: " Vorlesungsmanuskript Grundlagen der Raumfahrtsysteme," Institut fuer Raumfahrtsysteme (IRS) Universitaet Stuttgart, 1995.

Messerschmid, E.: "Grundlagen der Raumfahrtsysteme Formelsammlung," Institut fuer Raumfahrtsysteme (IRS) Universitaet Stuttgart, 2. Auflage, Feb. 1992.

APPENDIX

PICTURES OF THE EXPERIMENTS

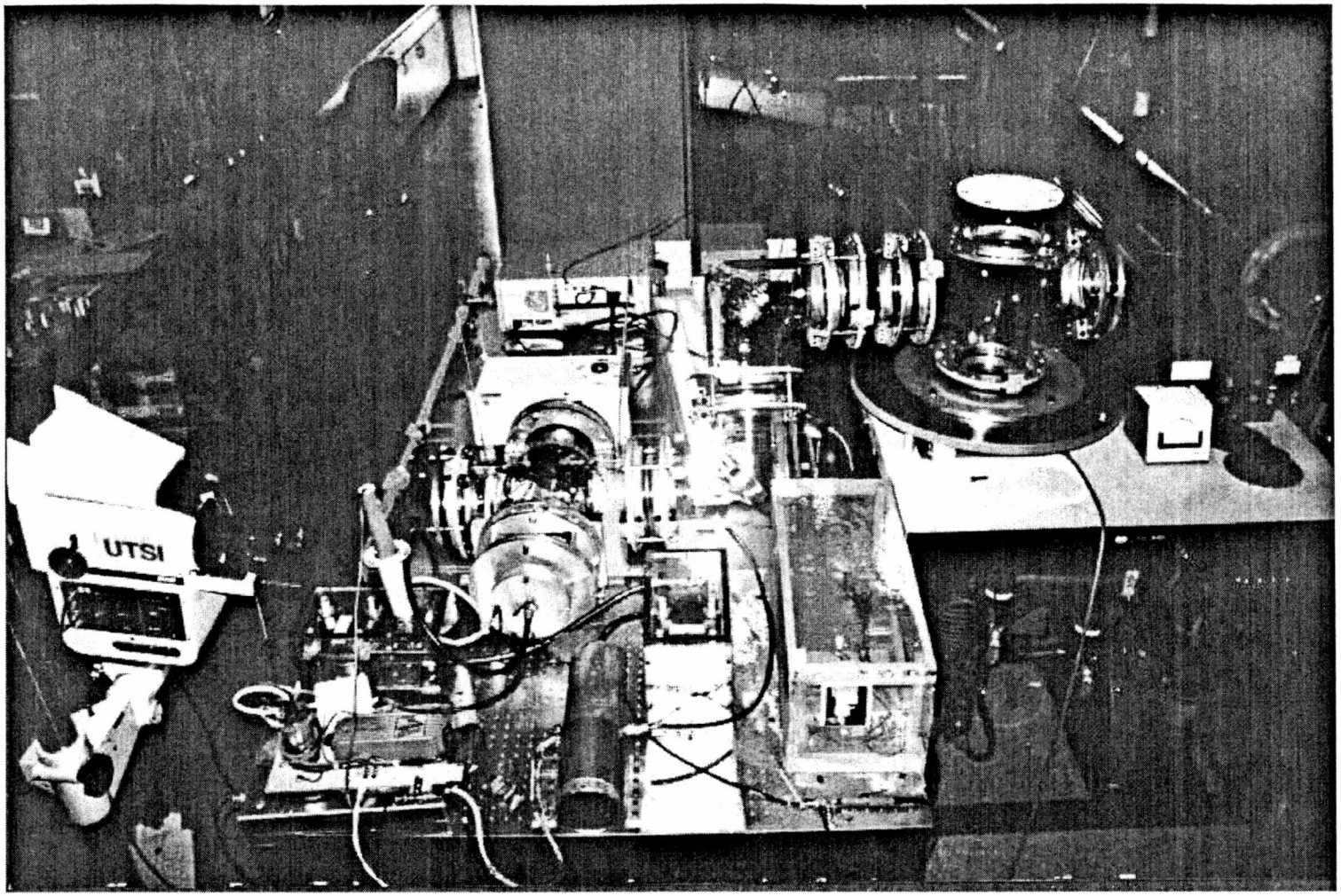

Plate A1: Experimental Setup

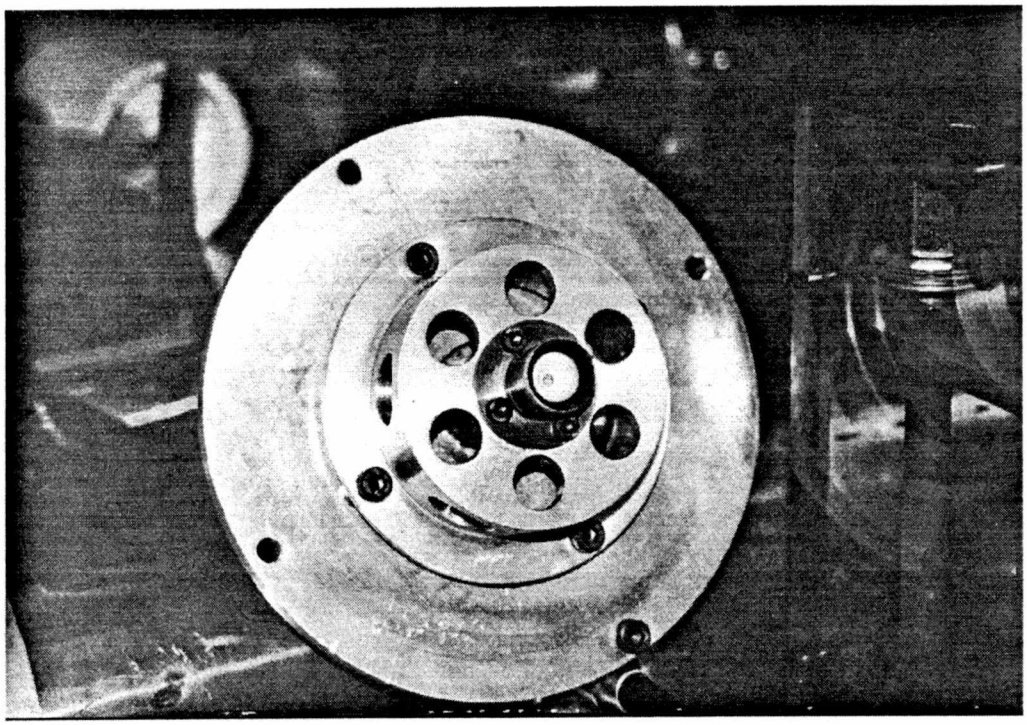

Plate A2: Picture of the thruster designed for the experiment.

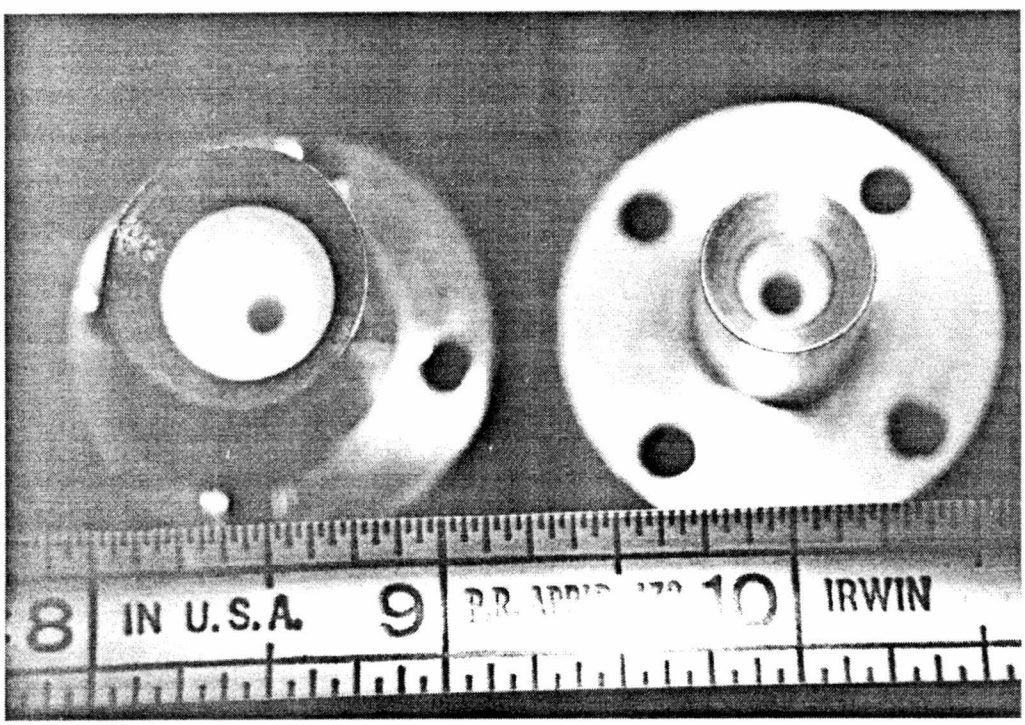

Plate A3: Large nozzle (left) compared to small nozzle (right).

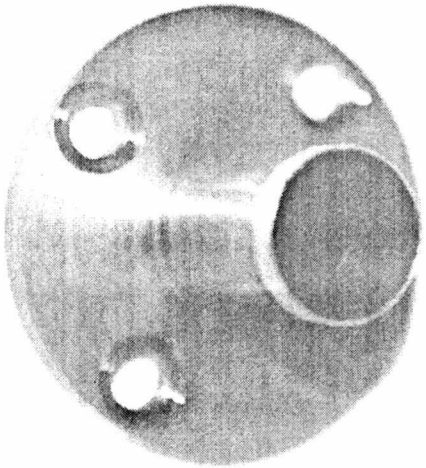

Plate A4: Picture of the small nozzle with the black soot layer at the inner nozzle walls.

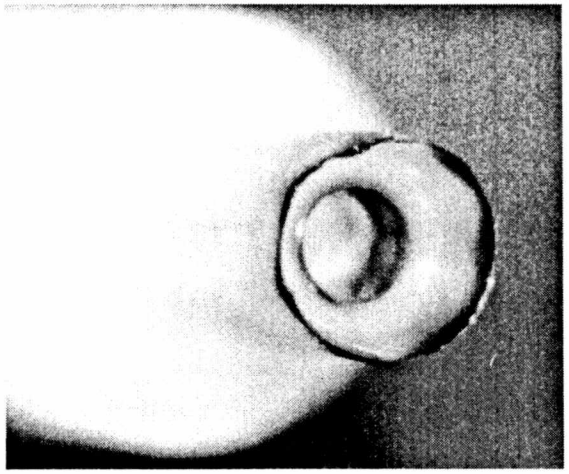

Plate A5: Picture of the ablation area of the propellant for the small nozzle.

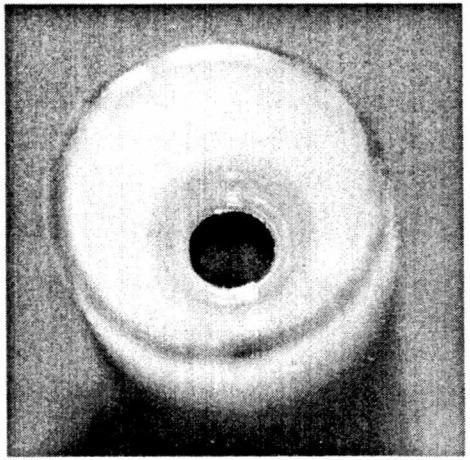

Plate A6: Picture of the ablation area of the propellant for the large nozzle.

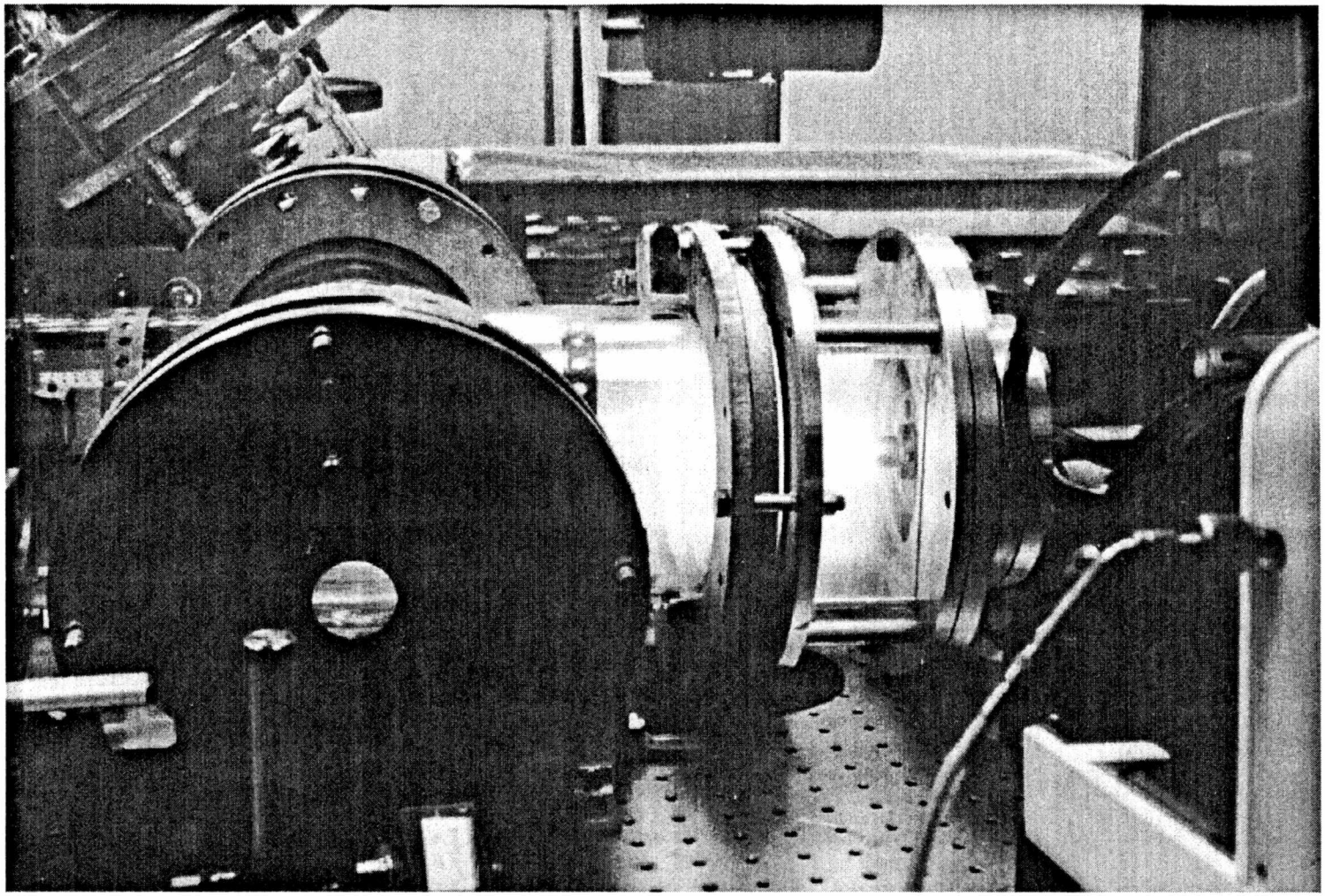

Plate A7: Picture of a shot as seen by an observer.

VITA

Thomas H. Walloschek was born April 17, 1973 in Schwaebisch Gmuend, Germany. He attended the Scheffold Gymnasium in Schwaebisch Gmuend from 1983 to 1989. Knowing that he was always interested in science and technology he transfered to the Technisches Gymnasium in Schwaebisch Gmuend for the last three years of his pre-university education. In May 1992 he graduated from the Technisches Gymnasium with the Allgemeine Hochschulreife (Abitur). He entered the University of Stuttgart, where he got his Vordiplom (similar to bachelors degree) in Aviation and Space Techniques, in May 1995. During his undergraduate studies he worked from November 1994 until March 1995 as an intern at Daimler Benz Aerospace Airbus in Hamburg where he was also able to visit Aerospatial Airbus in Toulouse, France. During his graduate studies at the University of Stuttgart he worked part time as a Graduate Research Assistant at the Institute for Space Systems.

He knew, that especially in the aviation and space market, a lot of the future projects would be established in international cooperation. For this reason, he decided to finish parts of his graduate studies in the United States and entered the graduate program of the University of Tennessee Space Institute in Tullahoma, University of Tennessee Knoxville, in August 1996. UTSI is well known by the Institute for Space Systems at the University of Stuttgart. Thomas pursued a Master of Science degree in Aerospace Engineering at UTSI where he worked as a Graduate Research Assistant to Dr. Dennis Keefer. The primary area of his research was electric propulsion,

especially coaxial thermal pulsed plasma thrusters. Thomas received his Master of Science Degree in May, 1998. He will finish his studies at the University of Stuttgart in Germany with a Diplom in Aviation and Space Systems in the near future.